A Step Toward Sustainability: Mechanisms of Hydrodeoxygenation Reactions over a Metal-Metal Oxide Catalyst

By

Kyle J. Stephens
B.Sc., University of Kansas, 2017

Submitted to the graduate degree program in Chemical Engineering and the Graduate Faculty of the University of Kansas in partial fulfillment of the requirements for the degree of Master of Science.

_____

Chair: Alan M. Allgeier

_____

Raghunath V. Chaudhari

_____

Aaron M. Scurto

Date Defended: 14 June 2019

The thesis committee for Kyle J. Stephens certifies that this is the approved version of the following thesis:

A Step Toward Sustainability: Mechanisms of Hydrodeoxygenation Reactions over a Metal-Metal Oxide Catalyst

Chair: Alan M. Allgeier

Date Approved: 19 June 2019

Abstract

In recent years, metal-metal oxide catalysts have proven to be robust catalysts for hydrodeoxygenation (HDO) of oxygenated compounds derived from bio-renewable feedstocks to value-added products. Herein, the conversion of 1,2,6-hexanetriol (1,2,6-HT) to 1,6-hexanediol (1,6-HD) in aqueous media over a Pt-WO_x/TiO_2 catalyst is examined via isotope incorporation in HDO of a model compound, 1,2-pentanediol (1,2-PD). Absence of a primary kinetic isotope effect (k_H/k_D = 0.84 ± 0.11) disproves a possible direct C–O scission mechanism. The observation of nearly complete deuterium incorporation in both the α-C and the β-C is inconsistent with the reverse Mars-van Krevelen mechanism and suggests an enol formation pathway that has not been proposed for HDO reactions of this type until now. Evidence consistent with the intermediacy of an oxocarbenium ion as a minor contributor has also been observed. In drawing the conclusions, it was necessary to characterize the facile isotope exchange between surface activated hydrogen and the water solvent. Hydrogenation of a water soluble olefin, tetra(ethylene glycol) diacrylate (TEGDA) in H_2/D_2O revealed predominant incorporation of deuterium instead of hydrogen in the reduced product, confirming the rapid exchange of surface activated hydrogen. The methods used in this study provide a new perspective for a reaction mechanism currently under debate, and these findings can be applied to other systems involving HDO of linear polyols over metal-metal oxide catalysts, improving catalyst design and utilization of sustainable feedstocks.

Acknowledgements

First, my praise goes to the **Lord** for making everything here possible. I recognize that all my strength, knowledge, and wisdom come from Him. I know all the wonderful people I am about to mention were placed in my path according to His design, and I cannot be more thankful for the blessings I have received, ones I do not deserve.

I thank my parents, **Scott** and **Karla**, and three sisters, **Katie**, **Jessy**, and **Sydney**, for always supporting me and showing me love, for always having a happy place to go home to, for having someone to go to when others let you down, and for being a family that is always enjoyable to be with. And so much more.

My gratitude also goes to my advisor, Dr. **Alan M. Allgeier**. His mentoring has made me into the researcher I am today by providing both high-quality expectations and supportive comments. To me, his position as an advisor is unparalleled. I also greatly appreciate his support in my future endeavors.

I would like to thank my coworkers, **Simon Velasquez-Morales**, **Vyoma Maroo**, and **Murilo Toledo Suekuni**, for being amazing people to work with. Our group's environment is not one that is often found, and I consider myself blessed to have all of you during this journey.

I thank my committee members, Dr. **Raghunath V. Chaudhari** and Dr. **Aaron M. Scurto**, for taking their time to revise this thesis and participate in my defense to provide comments that help me grow as a professional researcher.

I would like to recognize our neighbors, the research group of Dr. **Mark B. Shiflett**. They have been a fantastic group to work alongside. From the comradery of helping each other in the laboratory, to the fun outside of work, it has been a pleasure.

Appreciation also goes to Dr. **Sarah Neuenswander** and Dr. **Justin T. Douglas** of the KU NMR lab for providing invaluable assistance with NMR experimentation and data analysis. Also, I thank Dr. **Prem Thapa** of the KU Microscopy and Analytical Imaging lab for assistance and expertise with SEM and TEM imaging.

Table of Contents

List of Figures

List of Tables

List of Notations

1,2-HD = 1,2-hexanediol

1,5-HD = 1,5-hexanediol

1,6-HD = 1,6-hexanediol

1,2-PD = 1,2-pentanediol

1,2,6-HT = 1,2,6-hexanetriol

A = hydrogen

A^* = concentration of hydrogen at gas-liquid interface [kmol m^{-3}]

a_B = gas-liquid interfacial area per unit volume of the reactor [m^2 m^{-3}]

a_p = external surface area of catalyst per unit volume of the reactor [m^2 m^{-3}]

D = diffusivity of hydrogen in water [m^2 s^{-1}]

D_{eA} = effective diffusivity of hydrogen in catalyst pores [m^2 s^{-1}]

d_I = diameter of impeller [m]

d_p = catalyst particle diameter [m]

d'_p = screen diameter [m]

d_T = diameter of reactor tank [m]

h_I = height of impeller from bottom of reactor tank [m]

h_2 = height of liquid in reactor tank [m]

HDO = hydrodeoxygenation

k_L = gas-liquid mass transfer coefficient [m s^{-1}]

k_s = liquid-solid mass transfer coefficient [m s^{-1}]

l = diameter of impeller [m]

N = stirring speed [s^{-1}]

N_p = power number [--]

n = rps of impeller [rad s^{-1}]

P = catalyst porosity [--]

Pentanol = 1-pentanol

R_A = observed rate of hydrodeoxygenation reaction [kmol m^{-3} s^{-1}]

S_w = specific surface area of catalyst [m^2 g^{-1}]

Sc = Schmidt number [--]

Sh = Sherwood number [--]

THP2M = tetrahydropyran-2-methanol

V_g = volume of gas in reactor [m^3]

V_L = volume of liquid in reactor [m^3]

w = catalyst loading per unit volume of reactor [kg m^{-3}]

α_1 = gas-liquid mass transfer parameter

α_2 = liquid-solid mass transfer parameter

ε = rate of flow energy supply per mass of liquid [$m^2\ s^{-3}$]

ν = kinematic viscosity of solvent [$m^2\ s^{-1}$]

τ = tortuosity factor of catalyst [--]

ρ_p = catalyst particle density [$kg\ m^{-3}$]

ϕ_c = Carman's surface factor [--]

ϕ_{exp} = intraparticle mass transfer parameter

Chapter 1: Introduction

1.1 Biomass utilization

The utilization of biomass as a potential alternative for fossil resources in the production of chemicals and fuels has garnered significant attention in recent years. The chemical structure of different biomass species determine the type of fuels and valuable chemicals that can be derived from them and, accordingly, the functionalities and mechanisms that will be involved. Lignocellulosic biomass makes up about 90% of most plants by dry weight[1], and comprises cellulose, hemicellulose, lignin, and pectin. The first three are the components of greatest interest, as they are not associated with food production. Lignocellulose is composed of around 50% cellulose, 10-40% hemicellulose (10-30% in woods and 20-40% in herbaceous plants), and 10-40% lignin (20-40% in woods and 10-40% in herbaceous plants) on a dry basis.[2] The high degree of polymerization of cellulose provides strength to the plant cell walls while hemicellulose helps to bind this fibrous cellulose to the lignin, providing additional structural support as well as impermeability and resistance to microbial attacks.[3-4] Yang et al. observed the breakdown of these main constituents during pyrolysis and found that hemicellulose breaks down at 220-315 °C, cellulose at 315-400 °C, and lignin at 160-900 °C.[5] Accordingly cellulose contains stronger chemical bonds than hemicellulose, and lignin's broad temperature range is a product of its high degree of heterogeneity.

Cellulose is mainly found in plant cell walls that are part of stalks, stems, trunks, or any other woody portion of a plant, and it is also present in bacteria, fungi, algae, and even in some animals.[6] A great deal of literature has been produced on the structure and chemical properties of cellulose since its discovery and isolation from the rest of plant matter by Anselme Payen in 1838.[7]

It is a homogeneous, polymeric material, which forms a strong, fibrous structure. It is made of β-D-glucopyranose units, existing in chair formation, with its hydroxyl groups in the equatorial position; β-glycosidic bonds are responsible for the linkages within the polymer.[6, 8-9] The degree of polymerization for cellulose is about 10,000 for wood and 15,000 for cotton which cause this material to be insoluble in water.[10] Cellulose can be depolymerized to glucose monomers, which are used extensively in biomass utilization technologies.

Hemicellulose is a heterogeneous polymer with a much lower degree of polymerization than cellulose (~200)[11] with branched chains that may contain pentoses, hexoses, and uronic acid depending on the biomass source.[12] Xylan is the most prominent substance in hemicellulose that makes up anywhere from 8-25% of the total biomass weight,[13] and may be composed of a combination of arabinose and glucuronic, acetic, ferulic, and *p*-coumaric acids.[14] Xylans are typically heteropolysaccharides that are supported by homogeneous polymer chains of 1,4-linked β-D-xylopyranose units.[15] The sugar xylose can be obtained from hemicellulose just as glucose was from cellulose, and this can be used to produce various furans, which are some of the major building blocks for important biomass valorization products such as monomers and fuels.[16-17]

The quest for valorization of bio-renewable feedstocks and their derivatives requires technological developments ranging from the macro-scale, referring to processes of the chemical plant, down to the nano-scale of catalyst functionality and design. An aspect that aids in catalyst design is determination of the reaction mechanism,[18-20] and one important biomass reaction is the conversion of 1,2,6-hexanetriol (1,2,6-HT) to 1,6-hexanediol (1,6-HD).[21-23] 1,6-HD is a precursor to very popular polymers such as polyester,[24] polyurethane,[25] and Nylon-6,6,[26] and its procurement can be drawn from a few major renewable intermediates including isosorbide and hydroxymethylfurfural which can be derived from cellulose.[27-28] The central goal of this thesis is

the elucidation of the mechanism of 1,6-HD formation over $PtWO_x/TiO_2$ catalysts in aqueous media.

1.2 Metal-metal oxide catalysts

Metal-metal oxide supported catalysts have become popular in recent years for their superior activity in deoxygenation reactions that are important for biomass utilization.[21, 29] These reactions often involve the use of hydrogen as the reactive gas and water as the solvent. Water is a desirable solvent for its abundance and environmentally benign nature. An advantage of metal-metal oxide catalysts is their stability, both in structure and activity, under practical reaction conditions.[23, 30-32] Group VIIIB reducible metals paired with the transition metal oxides MoO_x, WO_x, and ReO_x are most commonly used, and form the epicenter of recent mechanistic investigations.[21, 23, 29, 32] The addition of a metal oxide greatly enhances the activity of the catalyst compared to traditional supported noble metal catalysts.[21, 29] The reason for this enhancement has proven elusive with some authors attributing it to the oxide/metal interface strengthening Lewis acidity.[33-34] Such structure sensitive catalysts must be carefully prepared to optimize the population of interfacial sites. In other work, a computational study showed a Ru/RuO_2 interface used for furfural hydrodeoxygenation (HDO) does not considerably enhance Lewis acid oxophilicity.[35] The Gibb's free energy of oxide formation, and hence reducibility, of the metal oxide is also an important factor governing activity and considered in catalyst optimization.[36]

The complexity of these catalysts has caused a definitive explanation of their function to be elusive. Group VIIIB metals are agreed to be responsible for hydrogen activation, but advocates for both homolytic and heterolytic dissociation exist.[35, 37] Also, whether the metal hydrides are involved in hydrogenation of the substrate is debatable.[38-39] Uncertainties about the functionality

of the metal oxide are also present in the community. As will be seen in the following sections, these sites have been argued to act as Brønsted acids in the form of surface hydroxyl species bound to the metal oxide which promotes acid catalyzed dehydration of the oxygenated substrate.[23, 38] However, if the metal oxide is characterized as a Lewis acid, oxygen vacancies are said to be formed at the metal oxide's surface enabling a reverse Mars-van Krevelen (RMvK) mechanism.[35, 39] Reducible supports such as TiO_2 are known to facilitate hydrogen spillover and transfer across their surfaces.[40] After H_2 activation, H atoms may travel in the form of proton and electron pairs, and in the case of the Pt/WO_3 system reduce W^{6+} species to W^{5+}.[41]

1.3 Mechanisms under consideration

To elucidate the mechanism of the selective HDO of 1,2,6-HT to 1,6-HD, four reaction pathways were considered. Three are derived from work of Dumesic,[38] Tomishige,[37] and Vlachos[35] and the fourth is a proposed acid catalyzed enol formation. All attempt to explain the deoxygenation pathway for various cyclic and linear oxygenates.

Dumesic and coworkers claim hydrogenolysis of both cyclic and linear oxygenates involves an oxocarbenium ion intermediate that precedes metal-catalyzed hydrogenation, seen in Figure 1.1.[38] Here, acid catalyzed dehydration occurs at the secondary C–O bond to form the carbenium intermediate following hydride transfer from the primary carbon. The resulting

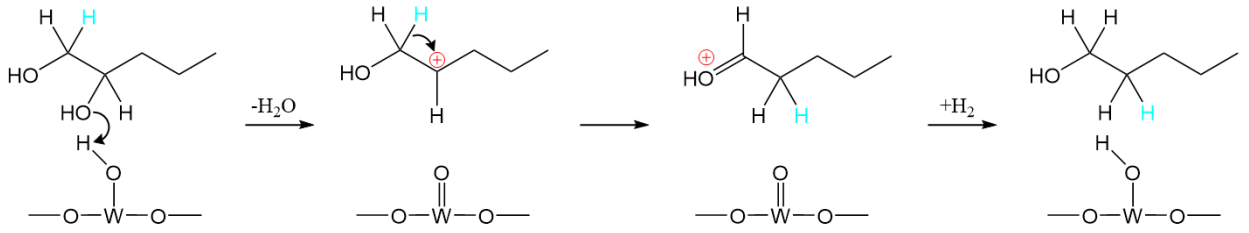

Figure 1.1: Reaction pathway via oxocarbenium ion formation derived from Dumesic and coworkers with WO_x species transformations.

oxocarbenium avoids formation of an unstable primary carbenium ion that would form if deoxygenation of the primary hydroxyl was executed. The unsaturated intermediate is then hydrogenated by a metal site, e.g. Pt-H species. The rate-determining step for this mechanism is expected to be the acid catalyzed C–O scission step. Brønsted acid sites on the metal oxide are regenerated via hydrogen spillover from Pt reducing W^{6+} to W^{5+}.[23]

The second mechanism under consideration is derived from that of Tomishige and coworkers.[37] Here a primary hydroxyl binding, followed by direct C–O scission is utilized to explain selectivity toward deoxygenation of the secondary hydroxyl. An adaption of this mechanism is seen below in Figure 1.2.

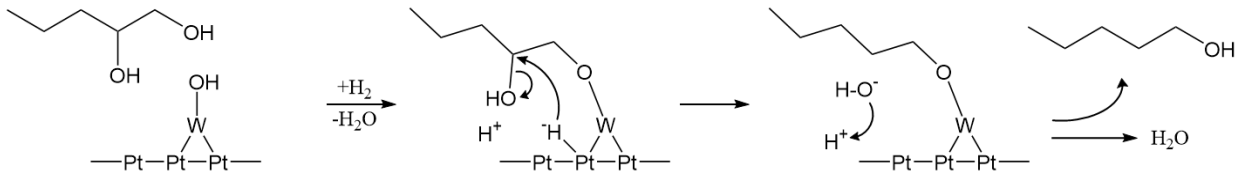

Figure 1.2: Reaction pathway via direct C–O scission derived from Tomishige and coworkers and catalyst surface transformations.

Pt is shown to heterolytically activate H_2 gas forming a H^- species at the metal oxide/metal interface and a H^+ ion in solution following Tomishige's precedent for $RhReO_x$. The H^- then reacts with the β-C of the substrate performing a direct C–O scission and forming the chemisorbed product while the leaving group forms water in solution. Metal oxide/metal interfaces are given much importance as the reaction is mediated by these sites. The rate-determining step of this mechanism is the surface reaction between the substrate and the H^- species.[37]

The RMvK mechanism is another plausible pathway for the present HDO reaction. Vlachos and coworkers have performed extensive computational studies on a Ru/RuO_x system for deoxygenation reactions[35] which could be relevant to the present system. Conversion of the substrate is dependent on oxygen vacancy formation in this mechanism. These vacancies are produced via reduction from hydrogen spillover. The steps are shown below in Figure 1.3. As

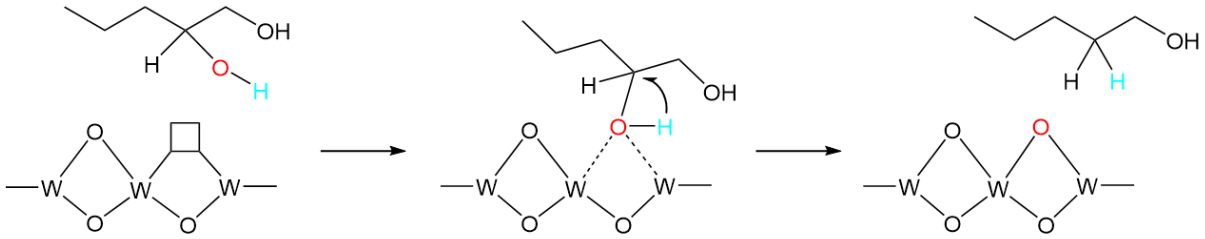

Figure 1.3: Reaction pathway via reverse Mars-van Krevelen derived from Vlachos and coworkers with oxygen vacancy transformations.

mentioned previously, cooperative interfacial sites are not given emphasis in the mechanism. Instead, oxophilicity and reducibility of the metal oxide is key for the performance of the catalyst.[35-36] After an oxygen vacancy is formed, the Lewis basicity of the substrate's secondary hydroxyl (which is greater than the primary hydroxyl) leads to preferred adsorption. After the C–O bond scission takes place, the vacancy is filled with the hydroxyl group as the substrate desorbs in the form of a radical followed by intermolecular H transfer from the adsorbed hydroxyl group.[35] Another plausible avenue is a concerted, two electron transfer from the vacancy site with concerted C–O bond scission which would form a very unstable carbanion intermediate. This carbanion would then quickly obtain a proton from the surrounding hydronium ions. The rate-determining step of this mechanism is deemed to be the breaking of the C–O bond. After the reaction takes place, oxygen vacancies are created again via reduction with hydrogen to repeat the cycle.

The fourth mechanism considered involves acid catalyzed dehydration followed by enol formation and alkene reduction and has some similarities to the first mechanism. Initial acid catalyzed dehydration is present in many proposals[23, 38, 42-43] with some proceeding to the oxocarbenium intermediate[23, 38] and others to ketones and aldehydes.[42] However, direct hydrogenation of the enol intermediate over Pt metal sites is a logical mechanistic step that was not promoted in the above three mechanisms. Following hydrogenation, the WO_x Brønsted sites are regenerated as in the oxocarbenium mechanism. Figure 1.4 below shows a possible reaction route via enol formation.

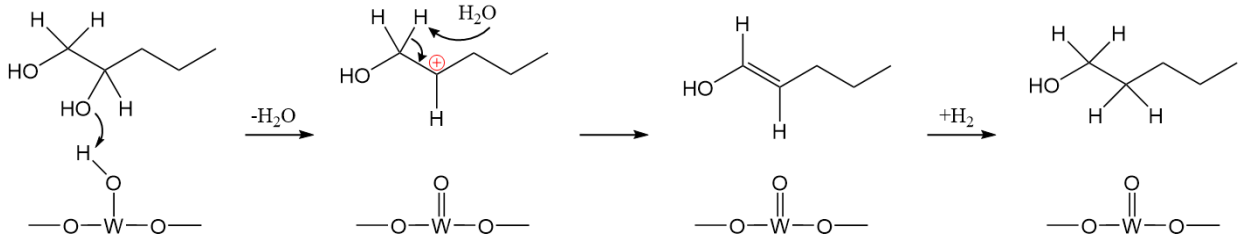

Figure 1.4: HDO reaction mechanism via acid catalyzed dehydration and enol formation.

Utilization of isotopologues, often hydrogen and deuterium, are invaluable for mechanistic studies, and in recent years deuterated compounds and D_2 gas have been employed in HDO investigations.[29, 44-45] Some experiments comprise deuterium incorporation into reaction products and are analyzed via nuclear magnetic resonance (NMR) spectroscopy to clarify the position of the differing isotope and make mechanistic deductions.[29, 45] Other experiments observe a kinetic isotope effect (KIE) that the heavier atom imposes on the reaction and gives clues on the nature of the rate-determining step.[44] Deuterium is often the isotope of choice because of its atomic weight ratio with hydrogen (2:1) allowing the largest differentiation among the accessible isotopes. In this work, the HDO mechanism of 1,2,6-HT conversion over Pt-WO_x/TiO_2 is elucidated. The techniques applied in this venture are: deuterium incorporation with D_2 gas and D_2O solvent, analysis of the rate of isotope exchange between the catalyst surface and solvent, and the observation of KIEs.

Chapter 2: Materials, Experimental Methods, and Characterization Techniques

2.1 Materials

The chemicals 1,2-pentanediol (96%), 1-pentanol (99%), methyl sulfoxide-d_6 (99.9 atom % D), and 1-methyl-2-pyrrolidinone were purchased from Acros Organics. 1,2,6-Hexanetriol (96%) and diethylene glycol diethyl ether (99+%), were purchased from Alfa Aesar. Deuterium oxide (99.9 atom % D), 1,2-hexanediol (98%), 1,5-hexanediol (99%), tetrahydropyran-2-methanol (98%), tetra-ammineplatinum(II) nitrate (# 278726) and ammonium paratungstate hydrate (# 510114) were purchased from Aldrich. Methanol (HPLC grade) was purchased from Fisher Scientific. Evonik Industries generously provided the TiO_2 catalyst support (Aeroxide P 25, # 99036028). Hydrogen (>99.9999%), deuterium (>99.999%), and carbon monoxide (99.999%) gases were purchased from Matheson Tri-Gas.

2.2 Catalyst synthesis

4 wt% Pt-WO_x/TiO_2 (1:1 Pt:W molar ratio), hereafter will be named Pt-WO_x/TiO_2, catalysts were synthesized via incipient wetness impregnation. First, a tetra-ammineplatinum(II) nitrate aqueous solution was added dropwise to wetted TiO_2 while being stirred vigorously. This mixture was then dried in a vacuum oven overnight at 110 °C. The dry solid was lightly rehydrated and an aqueous solution of ammonium paratungstate hydrate was added dropwise with vigorous stirring. The mixture was dried in a vacuum oven overnight at 110 °C. The dry solid was then calcined for three hours at 400 °C (5 °C min^{-1}). Pt/TiO_2 catalysts were synthesized following the same method except the steps involving the tungsten precursor were omitted. WO_x/TiO_2 catalysts were synthesized

following the same method omitting the Pt precursor where the same amount of WO_x loading as the previous catalysts was used.

2.3 Autoclave reactor

A custom-made autoclave reactor combined with a heating block and stirring magnet was used for screening reactions. The reactor is comprised of a stainless-steel rectangular base with a circular cutout that accommodates 7 x 1.5 mL reaction vials. Gases are introduced and exhausted through piping attached to a top plate that is secured to the base with bolts where a polytetrafluoroethylene (PTFE) gasket provides an air-tight seal between the plate and the base. The maximum allowable working pressure (MAWP) is 82 bar at 260 °C. Figure 2.1 below shows a schematic of the reactor where a legend can be found in Figure 2.3. It is equipped with an inlet accommodating multiple gases, a pressure gauge, a dual thermocouple (TC) that measures the temperature at the location of the reaction vials, and a rupture disk.

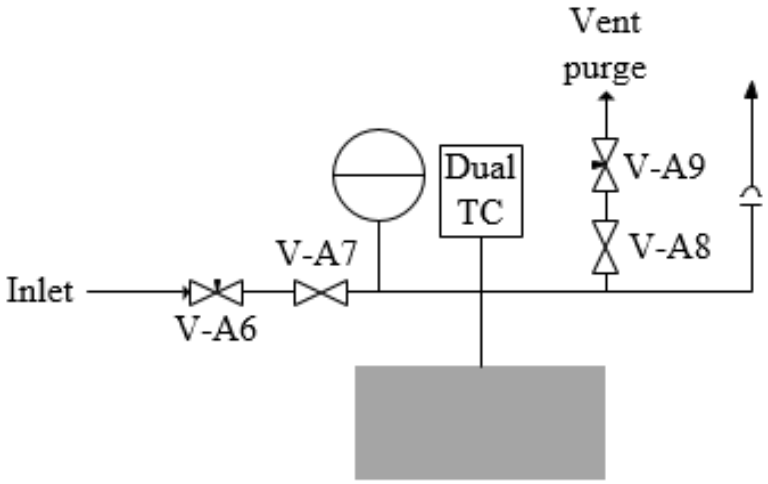

Figure 2.1: Schematic of autoclave reactor system.

The substrate solution and catalyst were charged with a PTFE stirring bar into a 1.5 mL glass vial closed with a metal cap and septum that was punctured with a needle to facilitate gas transfer. The vial was sealed in the reactor, purged with nitrogen followed by the reactive gas, and subsequently pressurized with the reactive gas. The reactor was then heated to the desired temperature and stirring was activated to initiate reaction. After the reaction, the reactor was cooled to room temperature and subsequently depressurized. The product solution was filtered from the catalyst and analyzed.

2.4 Stirred tank reactor

Kinetic studies were carried out in a 50 mL Parr Series 5500 Compact Reactor seen in Figure 2.2 where a legend can be found in Figure 2.3. This apparatus consists of a stainless-steel cup to which the reaction mixture is charged, and a stainless-steel head with multiple ports to accommodate an inlet, a dip tube for sampling, a rupture disk, pressure gauge, dual TC, and an outlet. The entire vessel is portable and is placed on a stand with a heating block and stir shaft. Heating and stirring

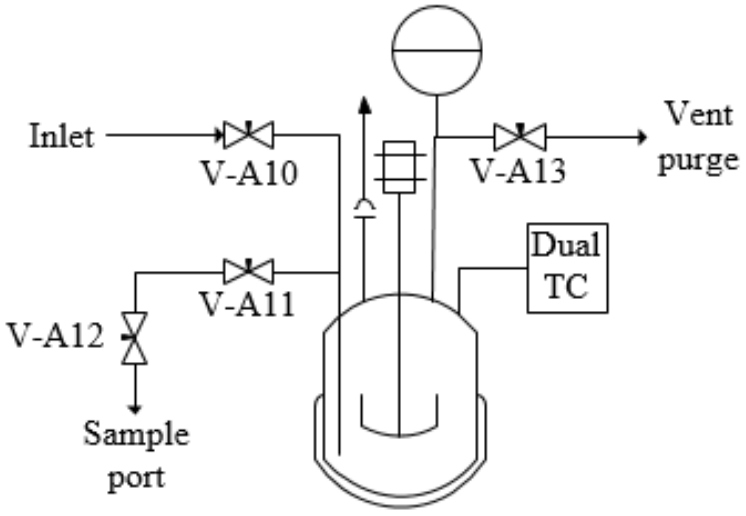

Figure 2.2: Schematic of stirred tank reactor system.

are controlled by a Parr Series 4848 Reactor Controller equipped with an over-temperature controller. The MAWP is 200 bar at 350 °C.

Substrate solution and catalyst were charged to the reactor, the reactor sealed, and purged with nitrogen followed by the reactive gas. The reactor was then pressurized with the reactive gas and heated to the reaction temperature with slow stirring. After reaching the desired temperature, the stirring was set to 1000 rpm initiating the reaction. Samples were taken during reaction by closing valve V-A12 and briefly opening valve V-A11 to trap a plug of liquid between the two valves. The liquid was allowed to cool before slowly opening valve V-A12 to avoid loss product via evaporation. Before each sample, 1 mL of product solution was purged through the sample line and discarded to ensure the line is clear of contaminants. After the reaction, the reactor was cooled to room temperature and pressure released.

Figure 2.3 below shows a piping and instrumentation diagram (P&ID) for both reactors. Compressed cylinders supplying the system with N_2, H_2, and an auxiliary gas are shown. The P&ID displays both reactors used; the braided hose is connected to the desired reactor's inlet during operation. A larger 150 mL stirred tank reactor is located beside the current setup which is operated via the side panel and air actuators mentioned in the diagram. Dual TCs are utilized for connections to both temperature controllers and over-temperature controllers for safety. Each reactor is fitted with a rupture disk to prevent over-pressurizing.

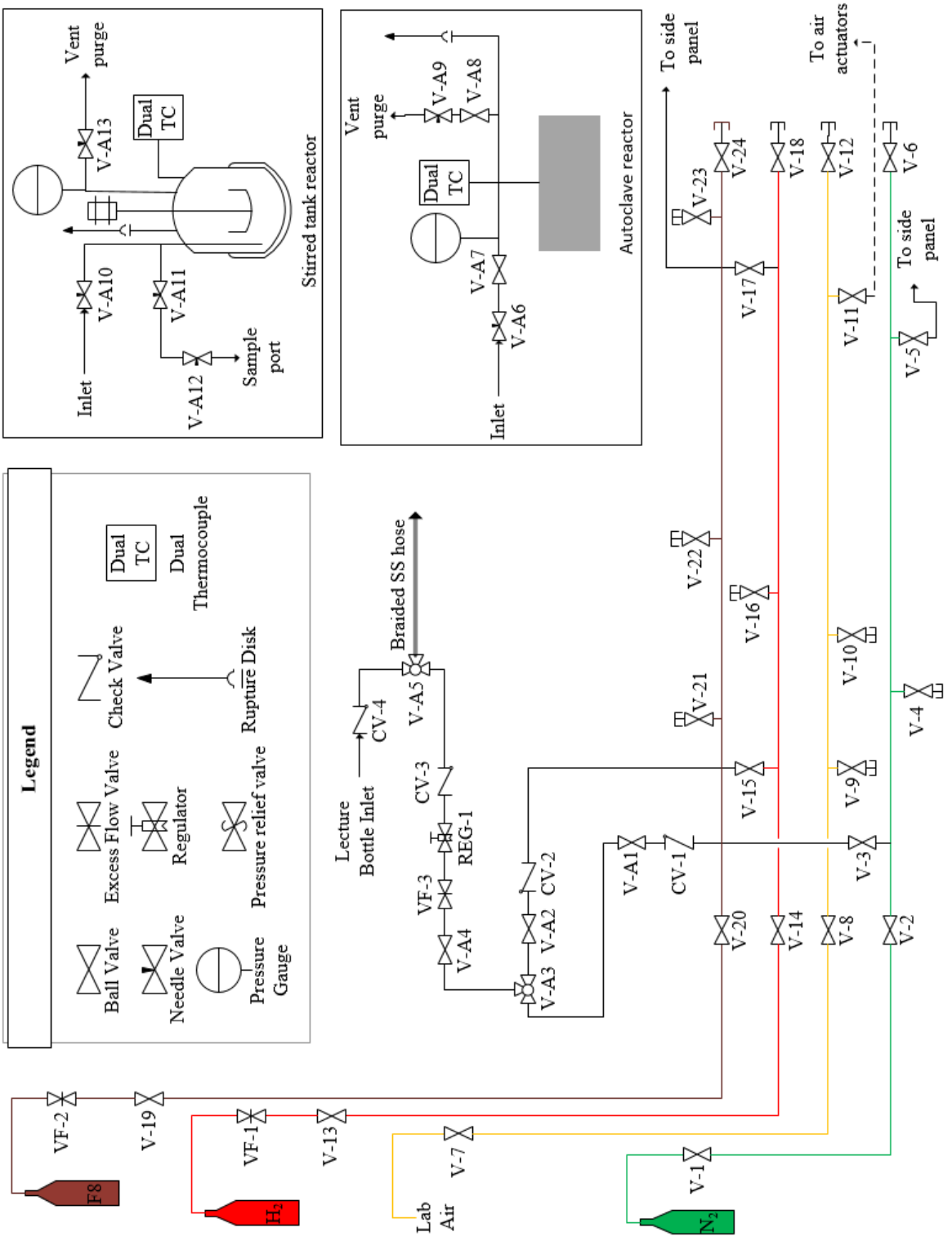

Figure 2.3: P&ID of the autoclave reactor and stirred tank reactor with upstream and downstream processes.

2.5 Gas Chromatography

Reaction product identification and quantification was done with an Agilent 7890B gas chromatograph (GC) equipped with an Rx-1701 column (30 m length, 0.25 mm internal diameter, and 1 μm film thickness) and a flame ionization detector (FID). Sample preparation involved filtering the product solution of particulates, addition of an internal standard, and dilution with methanol. Injections were made by an Agilent 7693A Automatic Liquid Sampler with 1 μL injection volume and a 10:1 inlet split ratio. Helium was used as the carrier and makeup gas. Calculations were made with an internal standard calibration (ISC) using diethylene glycol diethyl ether (Alfa Aesar # 43464) as the internal standard. All reaction data calculated with the ISC were compared to an external calibration of FID signal vs concentration with R^2 values >0.99 of a linear fit to the data points in the concentration range 0.1 – 6.0 mg mL^{-1}. An example of a reaction product injection can be found in Appendix A where all peaks are seen to separate and no overlapping occurs.

2.6 Nuclear Magnetic Resonance Spectroscopy

^{1}H and ^{2}H NMR analyses were performed with a Bruker Avance III HD 400 MHz resonator equipped with a broadband X-channel detect gradient probe. Analyses involving ^{13}C detection, including distortionless enhancement by polarization transfer – 135° (DEPT), were performed with a Bruker Avance III 500 MHz resonator equipped with a multi-nuclear BBFO cryoprobe. Reaction products were filtered from catalyst powder and inserted directly into a sample tube for analysis.

2.7 Powder X-Ray Diffraction

Powder x-ray diffraction (PXRD) was performed with a Bruker D2 PHASER equipped with a Co Kα radiation source (λ = 1.79026 Å) operated at 30 kV and 10 mA. The 2θ scanning angle ranged from 25° to 100° with a speed of 11°/min. Catalyst powders were loaded onto a poly(methyl methacrylate) specimen holder and pressed to level the powder surface with the holder to obtain highest reproducibility of data.

2.8 Scanning and Transmission Electron Microscopy

Scanning transmission electron microscopy (STEM) images were collected with an FEI Tecnai F20 field emission microscope equipped with a 200 kV electron source. Samples were suspended in ethanol via sonication and placed on a carbon Cu TEM grid. Scanning electron microscopy (SEM) images were collected with an FEI Versa 3D DualBeam SEM.

2.9 N_2 Physisorption

N_2 physisorption was performed on a Micromeritics ASAP 2020 Plus Chemisorption apparatus. Before analyses, samples weighing about 0.2 g were degassed for 12 hours at 150 °C under vacuum (<0.1 Torr). Measurements were taken of adsorbed gas at liquid nitrogen temperatures (-196 °C) at relative pressures of N_2 ranging from ~0.050 to ~0.988 Relative pressure is defined as P/P_o which is the absolute pressure over the saturation pressure. Surface areas were calculated by the Brunauer-Emmett-Teller (BET) theory; equations and error analysis can be found in Appendix E. Pore size distributions were found using the method of Barrett, Joyner, and Halenda (BJH) which

is an iterative algorithm used in the software to analyze the adsorption and desorption isotherms seen in Appendix E. This method was used since the material is in the mesoporous regime.

2.10 CO Chemisorption

Carbon monoxide chemisorption experiments were conducted with a Micromeritics ASAP 2020 Plus Chemisorption apparatus. About 0.3 g of catalyst was placed in a quartz sample tube supported by quartz wool above and below the sample to prevent entrainment. First, the sample was heated to 100 °C under vacuum for 30 minutes and backfilled with He. Then, the samples were subsequently heated to 350 °C under the flow of H_2 for 120 minutes to reduce the catalyst. After evacuation, the sample tube was cooled to 35 °C under vacuum, an automated leak test of the system was done, and another evacuation performed. Isothermal analysis with CO was done at 35 °C with 8 pressure data points ranging from ~100 mmHg to ~450 mmHg; this first analysis measures both physisorbed and chemisorbed CO. A repeat analysis was done on the resulting unreduced catalyst in which only the physisorbed CO was measured, CO molecules adsorbed to surface species other than Pt, and this amount was subtracted from the results of the first analysis to give a value that represents only chemisorbed CO. Equations used for calculating metal dispersion and metal surface area are found in Appendix F.

Chapter 3: Results and Discussion

3.1 Catalyst Characterization

3.1.1 Powder X-Ray Diffraction

To analyze the crystal structure of different components of the catalyst, PXRD was performed. Figure 3.1 shows patterns of three catalysts: Pt-WOx/TiO_2, Pt/TiO_2, and WO_x/TiO_2 as well as the support, TiO_2. The TiO_2 support was subjected to the same synthesis conditions and thermal history as the catalysts to enable use as a control. There are noticeable peaks at ~46° and ~54° on

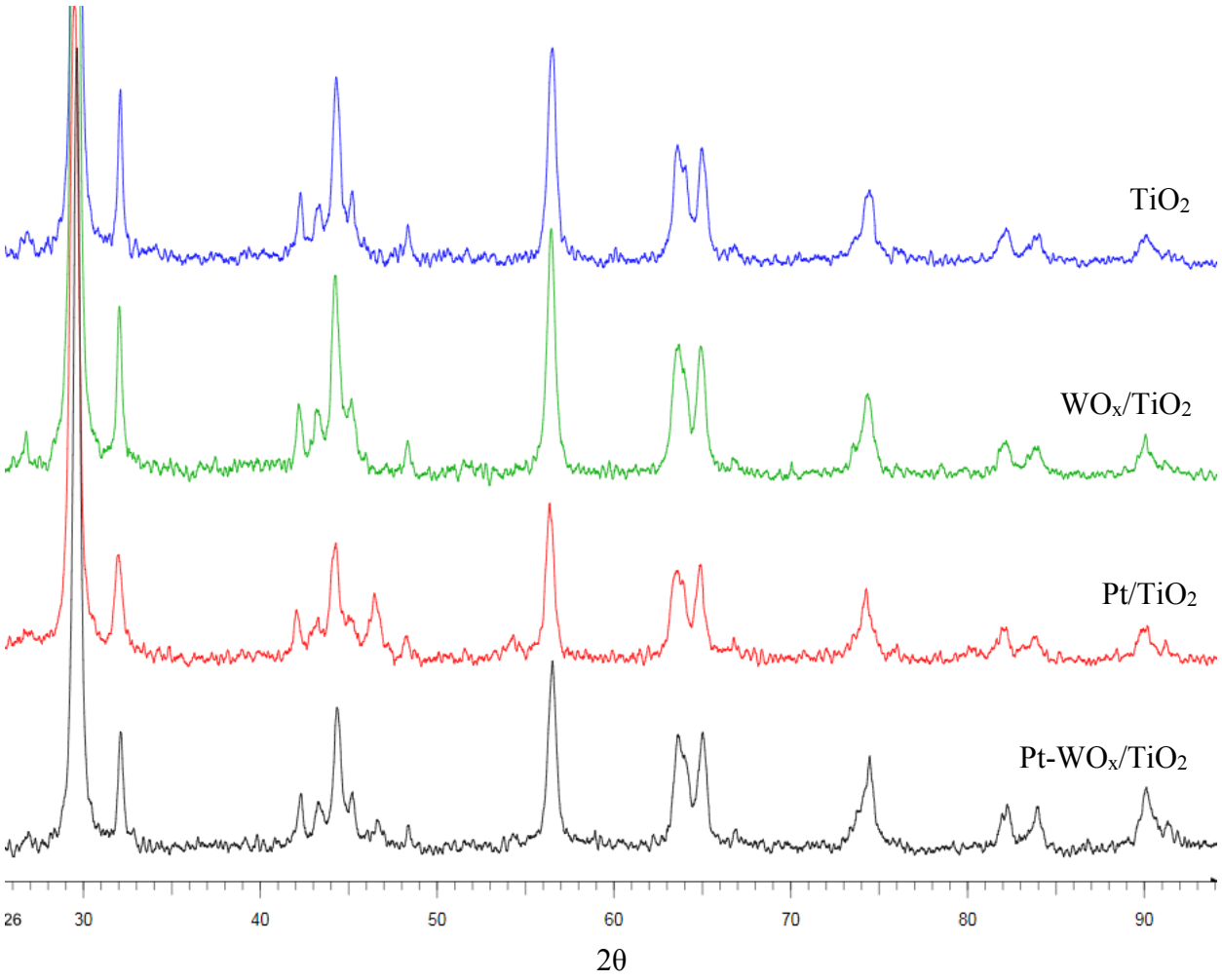

Figure 3.1: XRD patterns of Pt-WO_x/TiO_2 (black), Pt/TiO_2 (red), WO_x/TiO_2 (green), and TiO_2 (blue).

the two platinum-containing catalysts that correspond to Pt (111) and (200) respectively.[46-47] The Pt-WO_x/TiO_2 catalyst Pt peaks are seen to be smaller than that of the Pt/TiO_2 catalyst, consistent with the decreased metallic surface area seen in CO chemisorption (Section 3.3.2). The patterns of tungsten oxide-containing catalysts were fitted with peak profiles for WO_2 and WO_3 and no apparent matching was seen (Appendix C), but the surfaces of TiO_2 nanoparticles are visibly altered by the addition of WO_x (Figure 3.2d) which indicates WO_x is very well dispersed. Quantitative analysis of the TiO_2 phase for each catalyst gave a composition of ~90% anatase and ~10% rutile via relative peak intensities.

3.1.2 Scanning and Transmission Electron Microscopy

TEM was performed on the catalysts for qualitative analysis. The results compliment other characterization data. Figure 3.2 shows the Pt nanoparticles to be on the scale of 2 to 3 nm which is consistent with the same catalyst found in literature.[23] However, the Pt nanoparticles seem to be

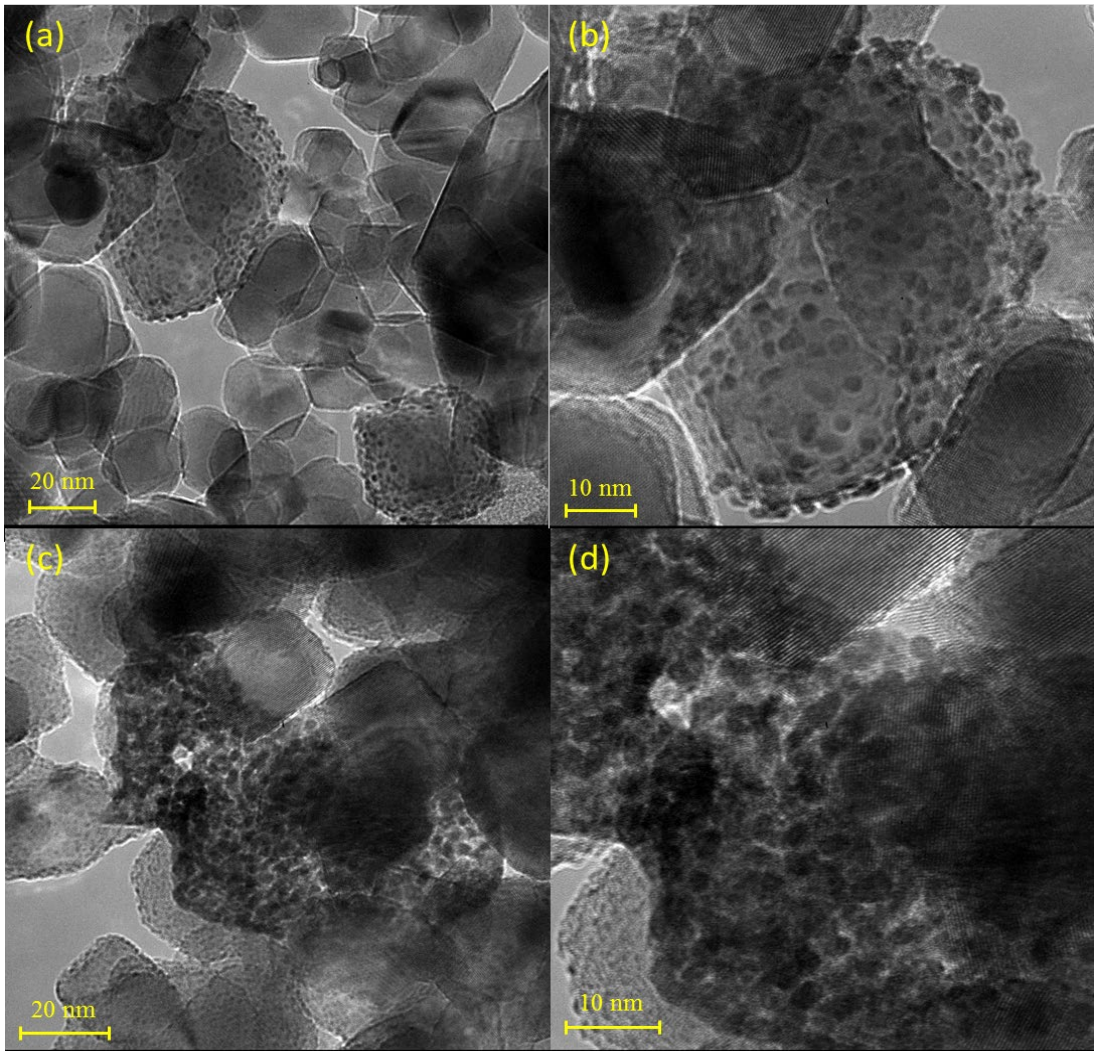

Figure 3.2: TEM images of 4 wt% Pt/TiO_2 at (a) 20 nm and (b) 10 nm length scales, and of $Pt\text{-}WO_x/TiO_2$ at (c) 20 nm and (d) 10 nm length scales.

selectively growing on certain TiO_2 particles suggesting there is a preferred phase of growth for platinum. The surface of TiO_2 particles are visibly altered by the addition of WO_x (compare Figure 3.2b and d), and since reactivity is affected by the addition of WO_x, but its presence not detected

by PXRD, it can be said that the sub-nanometer roughness observed on TiO_2 in TEM imaging is attributable to highly dispersed WO_x. Also, Appendix D shows the same roughness for a WO_x/TiO_2 catalyst, suggesting roughness is not a contribution from Pt.

Appendix D contains an SEM image at 500 μm length scale that shows Pt forming concentrated clusters in various areas. It has been proposed in literature that Pt has a tendency to nucleate on the rutile phase as opposed to the anatase phase of TiO_2[48] which could explain the clustering seen in TEM and SEM imaging. It should be noted that the Pt particles remain separate from one another and do not agglomerate into large single particles.

3.1.3 N_2 Physisorption

Catalyst surface area and pore size distribution were found for the Pt-WO_x/TiO_2 catalyst via N_2 physisorption. The results are seen in Table 3.1 below. The BET surface area is in agreement with values in the literature.[23] The average pore diameter shows that the material is in the mesoporous region which is why the BJH method was used for the calculations. An isotherm plot of adsorbed N_2 versus relative pressure can be found in Appendix E.

Table 3.1: N_2 physisorption results for Pt-WO_x/TiO_2 catalyst.

BET surface area ($m^2\ g^{-1}$)	BJH cumulative pore volume ($cm^3\ g^{-1}$)	BJH average pore diameter (nm)
53.8 ± 0.3	0.38 [a]	29.3 [a]

[a] Experience with this technique suggests that most samples have an uncertainty less than 5% of value.

A pore volume distribution has not yet been reported for the Pt-WO_x/TiO_2 catalyst. N_2 adsorption and desorption isotherm data can be found in Figure 3.3 where the data are plotted as change in pore volume over change in pore diameter as a function of pore diameter. Both adsorption and desorption isotherms show that a large population of pores lie in the 5-80 nm diameter region, and another population is seen around 2 nm in diameter in the adsorption isotherm (Figure 3.3a).

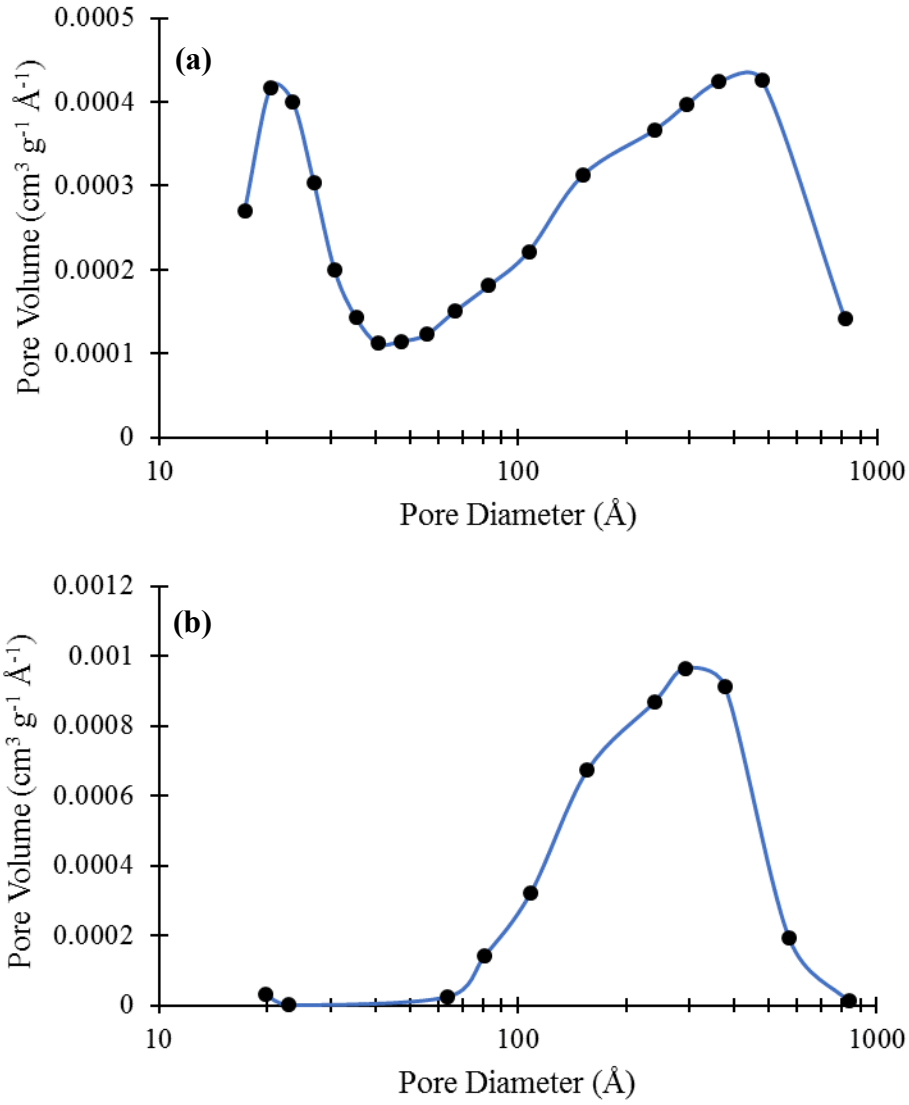

Figure 3.3: BJH pore volume distributions of the Pt-WO_x/TiO_2 catalyst of N_2 (a) adsorption isotherm and (b) desorption isotherm.

3.1.4 CO Chemisorption

To obtain Pt metal dispersion and surface area CO chemisorption was performed. The Pt-WO_x/TiO_2 catalyst was compared with a 4 wt% Pt/TiO_2 catalyst to observe the effects of added WO_x. These results can be found in Table 3.2.

Table 3.2: CO chemisorption results for Pt-WO_x/TiO_2 and 4 wt% Pt/TiO_2 catalysts.[a]

Catalyst	CO uptake (μmol g^{-1})	Metal dispersion (%)	Metallic surface area (m^2 g^{-1})
Pt-WO_x/TiO_2	10	5	0.5
4 wt% Pt/TiO_2	19	9	0.9

[a] Experience with this technique suggests that most samples have an uncertainty less than 15% of value.

All values found in Table 3.2 decrease with the addition of WO_x. The group of Huber characterized the Pt-WO_x/TiO_2 catalyst and found that there is a volcano plot relation between WO_x loading and turnover frequency of a Pt-WO_x/TiO_2 catalyst for hydrogenolysis of tetrahydrofuran-2,5-dimethanol.[23] Wang et al. showed that WO_x creates a submonolayer film over Pt nanoparticles which is characterized as the active region.[49] The chemisorption results in Table 3.2 support this idea since the Pt-WO_x/TiO_2 catalyst has less CO uptake than Pt/TiO_2 even though both catalysts have the same Pt loading. WO_x seems to be depositing partly on the Pt nanoparticles.

3.2 Hydrodeoxygenation of 1,2,6-Hexanetriol

As mentioned previously, production of 1,6-HD via HDO of 1,2,6-HT is a beneficial route due to the use of a sustainable feedstock. Also, application of the supported metal/metal oxide catalyst, 4 wt% Pt-WO_x/TiO_2 (1:1), invented by Allgeier et al.[22] of DuPont, gives high conversion and selectivity to 1,6-HD. The deceptively simple reaction scheme is show below in Scheme 3.1.

Scheme 3.1: HDO of 1,2,6-HT to 1,6-HD over a Pt-WO_x/TiO_2 catalyst.

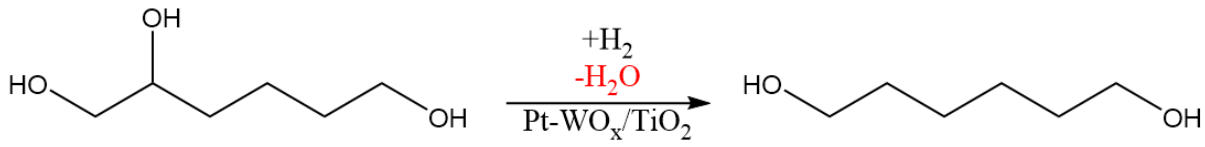

The activity of the catalysts synthesized for this study were compared to that of the patent using the same reactor type and conditions. Data for these are seen in Table 3.3. The conversion values are very similar, but the selectivity to 1,6-HD for the catalysts in this work is a bit lower. Since this difference is not very significant and the catalysts are still quite selective for the α,ω-diol product, the catalysts synthesized were deemed satisfactory for mechanistic studies.

Table 3.3: Comparison of DuPont patent to this work's reaction results for HDO of 1,2,6-HT.[a]

Source	1,2,6-HT Conversion (%)	1,6-HD Selectivity (%)
DuPont patent[22]	86	84
This work	89	70

[a] Reactions for both works were performed in an multi-well pressure reactor using a 1.5 mL vial with 1 mL of substrate solution (5 wt% 1,2,6-HT in H_2O) at 180 °C under 69 bar H_2 for 4 hours.

The autoclave reactor was used to collect data for five reactions ranging from 30 minutes to 4 hours. This was done since the apparatus does not allow sampling during the reaction. Products

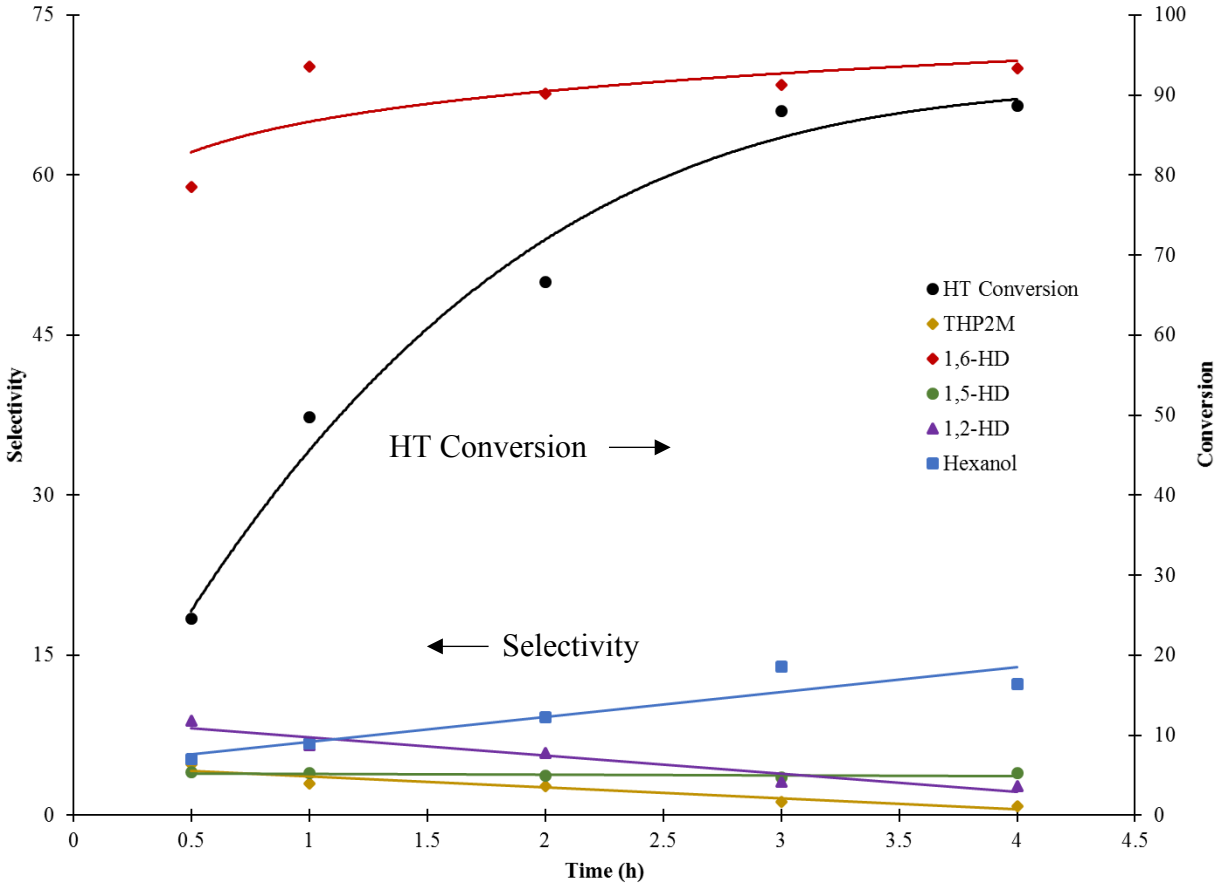

Figure 3.4: Conversion and selectivity data for HDO of 1,2,6-HT in the autoclave reactor. Note: each data point is a separate reaction run for the specified time. Each reaction contained 1 mL of substrate solution (5 wt% 1,2,6-HT in H2O) in a 1.5 mL pressure vessel operated at 180 °C under 69 bar H_2. The reaction at 4 h was repeated 7 times and an error of ±1.8% was found for 1,2,6-HT conversion and ±0.72% for 1,2-PD selectivity.

of each reaction were analyzed by GC and quantified with an internal standard method. Conversion of 1,2,6-HT and selectivity to 1,6-HD and byproducts: tetrahydropyran-2-methanol (THP2M), 1,5-hexanediol (1,5-HD), 1,2-hexanediol (1,2-HD), and 1-hexanol (hexanol) are shown in Figure 3.4. The results show the selectivity to 1,6-HD is ca. 70% at fairly high conversion. As described in Section 1, the mechanistic assertion of Dumesic et al.[38] explains this observation by noting

formation of a secondary carbenium versus a primary carbenium is more stable, thus favoring deoxygenation of the secondary hydroxyl. In one description of the direct C−O scission mechanism, the anchoring of the substrate by its primary hydroxyl to the oxophilic metal would direct the secondary C–O bond to the noble metal H^- species, logically explaining the selectivity.[37] A RMvK mechanism[35] would attribute selectivity to secondary hydroxyl cleavage due to stronger Lewis basicity of the secondary hydroxyl leading to preferred association to the reduced vacant site of WO_x. Beyond the desired reaction manifold it will be noted that THP2M can be formed via acid catalyzed ring-closure of 1,2,6-HT[21] (even during heat up), but ultimately re-opened and deoxygenated as seen with the decreasing selectivity to THP2M. Selectivity to 1,5-HD and 1,2-HD also decrease as they readily convert to hexanol, which is seen to increase with time. For the desired reaction pathway that produces 1,6-HD each of the mechanisms described above provides a rationale for the selective reduction at the secondary alcohol site but each would lead to alternate perspectives on how to optimize the catalyst, e.g. tuning density and strength of acid sites, versus tuning the reducibility of the oxophilic metal sites. Accordingly, elucidation of the operative mechanism of great value.

3.3 Deuterium Incorporation

3.3.1 Deuterium Incorporation of 1,2-Pentanediol

Deuterium incorporation in HDO reactions using D_2 as the reactive gas or D_2O as the solvent has shown to be insightful for mechanistic investigations involving phenolic compounds.[45, 50] Similar methodology to evaluate the reaction pathway for the conversion of the compound of interest, 1,2,6-HT, has been implemented in this investigation. However, HDO of 1,2,6-HT yields a symmetrical molecule, 1,2-HD, proved challenging to analyze via NMR as two pairs of C atoms

would possess the same chemical shift. A substrate that yields an asymmetrical product upon HDO was desirable to simplify NMR analysis. HDO of 1,2-PD with Pt-WO_x/TiO_2 selectively yields 1-pentanol (pentanol) where each carbon atom has a unique chemical shift, and this molecule can be considered similar in reactivity of 1,2,6-HT since they both contain neighboring primary and secondary hydroxyls on a carbon chain. Therefore, 1,2-PD was used as a model compound in our mechanistic studies.

Experimental permutations, involving substituting the reactive gas, hydrogen, or solvent, water, with its corresponding isotopologue; D_2/H_2O (**A**) and H_2/D_2O (**B**) were conducted. Scheme 3.2 shows the expected deuterium positions upon incorporation using system **A** for each mechanism in consideration. It will be noted that no attempt to analyze the hydroxyl protons was made as these are expected to rapidly scramble with the water solvent. The oxocarbenium formation suggested by Dumesic and coworkers has two possible products, but the intermediate yielding compound RCH_2-CHD-OH (**1**) seen in Scheme 3.2 was shown, computationally, to be more favorable.[38] A compound with the formula RCHD-CH_2-OH (**2**) arises from the direct C-O scission derived from the mechanism of Tomishige and coworkers[37] and is regarded as the main product of this route. A RMvK pathway yields RCH_2-CH_2-OH (**3**), no incorporation from the gas, since the primary function of the deuterium drawn from the gas is to create oxygen vacancies via dissociation of deuterons and electrons and, following the precedent of Vlachos and coworkers,[35] the substrate abstracts a hydrogen radical from the departing hydroxyl. Enol formation gives way to the α-C and β-C, both being deuterated on the metallic, Pt surface of the catalyst giving RCHD-

CHD-OH (**4**). From this perspective, isotope incorporation would provide definitive evidence for which mechanism is operative under the present conditions.

Scheme 3.2: Expected deuterium placement after incorporation in D_2/H_2O system over Pt-WO_x/TiO_2 for each considered mechanism.

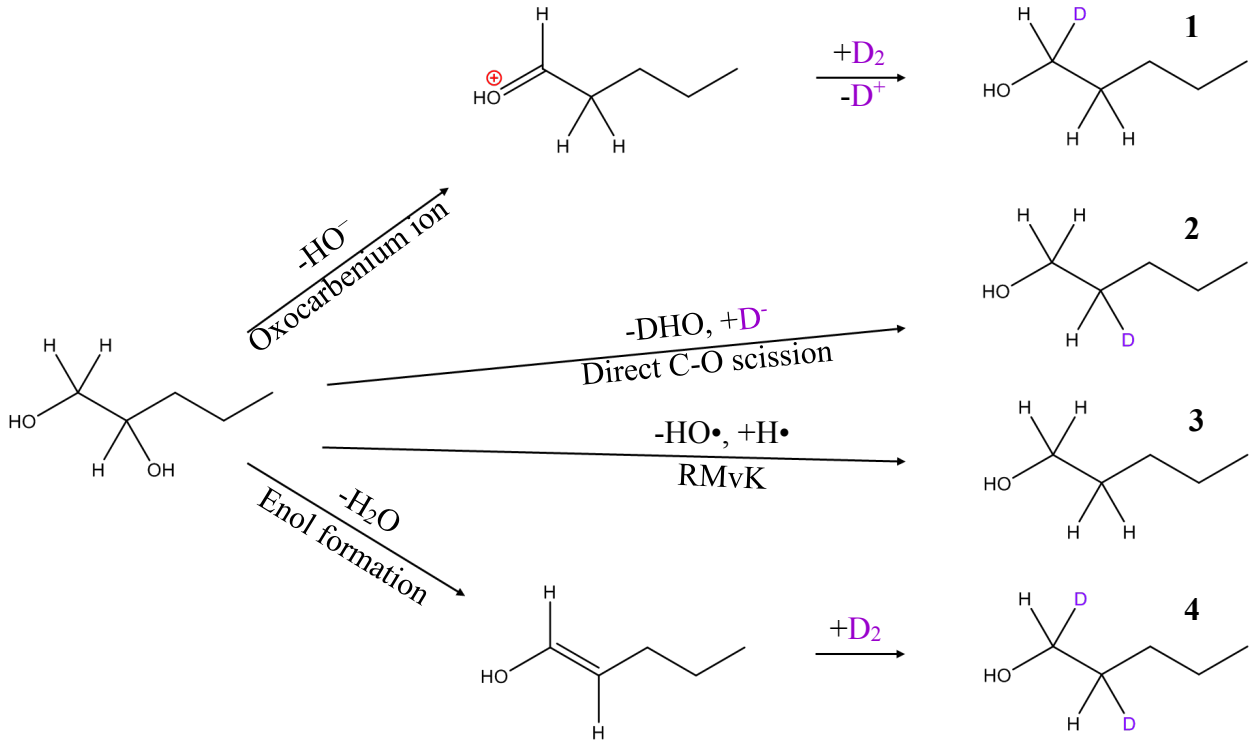

Using the methodology previously described, the mechanism of selective HDO of the secondary hydroxyl on 1,2-PD over Pt-WO_x/TiO_2 was investigated. The product solution was analyzed by NMR to characterize the position of deuterium atom incorporation into the product. This was accomplished by utilizing the DEPT technique paired with a separate integratable ^{13}C NMR. The integratable ^{13}C NMR experiment was set up to allow sufficient delay time to allow full relaxation between scans. Peaks were assigned to each carbon atom of the product in the ^{13}C spectrum and the corresponding peak in DEPT was used to determine the number of H atoms bonded to each carbon. This is done by a pulse sequence containing multiple timed pulses on the

carbon and proton channels. Experiments in this study use an initial 90° pulse angle on the ^{1}H channel and a final ^{1}H pulse angle of 135° to cause CH and CH_3 species to have a different phase than CH_2 species. Quaternary carbons to not appear in the spectra. Also, the sequence contains a time period between the first 90° proton pulse and the final pulse where spins evolve under the one-bond scalar coupling between the carbon atom and its protons. This transfers spin order from the more highly polarized protons to the carbon atoms which increases the carbon signal intensity.[51]

After the number of H atoms, and thus the number of D atoms, were determined for each carbon, the peaks of interest were then integrated using the ^{13}C spectrum and relative amounts of each species calculated. Splitting patterns in the ^{13}C spectrum were consistent with the substitution patterns predicted by DEPT. Figure 3.5 depicts this method analyzing the beta-carbon (β-C) of pentanol resulting from HDO of 1,2-PD over Pt-WO_x/TiO_2 with the reaction permutation **B** under 50 bar H_2 pressure at 180 °C in the stirred tank reactor. Here, two singlets are seen at ~30.87 ppm and ~30.75 ppm which correspond to a -CH_2- species since the DEPT spectrum shows a negative phase. There are two peaks present because differing isotopologues (adjacent carbon) cause a deuterium induced ^{13}C shift.[52] Integration of both peaks includes C atoms from all pentanol isotopologues consisting of a -CH_2- species at the β-C. Two triplets are present ranging from 30.15 ppm to 36.50 ppm that are assigned to a -CHD- species since the DEPT spectrum shows positive values. Two sets of triplets are seen due to the effects mentioned previously.[52] Proton decoupling prevents additional splitting from arising in ^{13}C spectra, which is why the carbons with only H atoms bonded are present as singlets. However, carbons with one D atom appear as triplets because the NMR experiments were not deuterium decoupled. NMR spectral regions of the α-C, as well as, results from permutation **B** can be found in (Appendix B). Each peak was fitted with a Gaussian

integral which enables integration of partially overlapping peaks. The areas were summed, and a percentage of each species was determined.

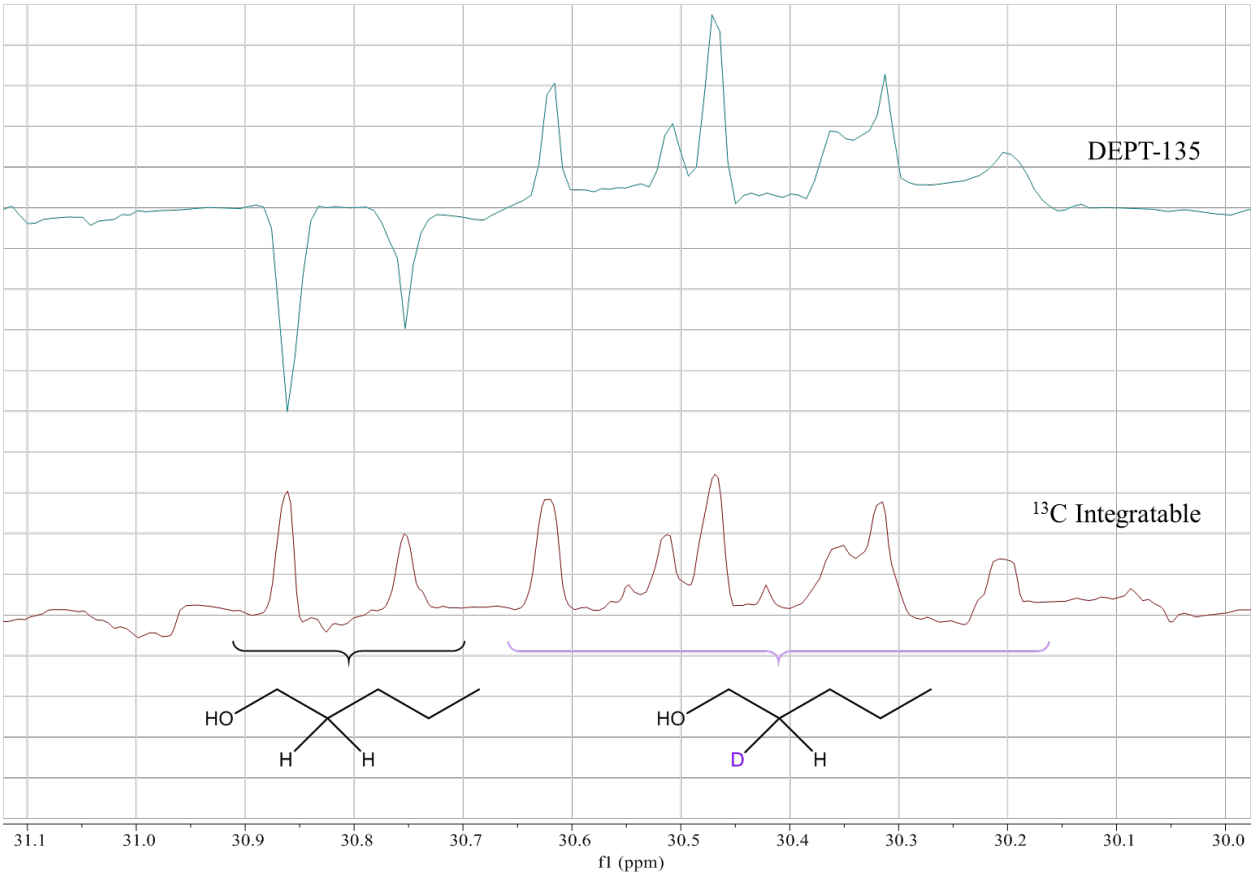

Figure 3.5: NMR analysis on the β-C of pentanol after HDO of 1,2-PD with the H_2/D_2O reaction system.

Table 3.4 below shows the results of deuterium incorporation of 1,2-PD HDO for both reaction permutations.

Table 3.4: Results of deuterium incorporation reactions of 1,2-PD HDO.[a]

Reaction system (gas/solvent)	α-C		β-C	
	$-CH_2-$	-CHD-	$-CH_2-$	-CHD-
D_2/H_2O (A)	100%	0%	100%	0%
H_2/D_2O (B)	0%	100%	19%	81%

[a] Reactions were performed with 25 mL of aqueous substrate solution (5 wt% 1,2-PD) in the stirred tank reactor at 180 °C under 50 bar of reactive gas with 1.0 g Pt-WO_x/TiO_2 and 4 h reaction time.

For permutation **A**, the α-C and β-C were each bonded to two H atoms, i.e. compound **3** was the only product**.** For the other permutation (**B**), opposite incorporation was observed at the α-C and largely for that of the β-C. The installation of permutation **A** supports the RMvK pathway since only hydrogen is seen at α-C and β-C, **3**. However, this mechanism cannot explain the incorporation seen in permutation **B** since only the β-C should have been labeled with deuterium.

While working with such gases paired with a protic solvent, one must be wary of isotope exchange reactions between H and D of the catalyst surface and the solvent.[53] Also, isotopic exchange between the solvent and the substrate or products can occur. These complications are evaluated in the following section.

3.3.2 Isotope Exchange Analyses

After each reaction in Section 3.3.1, the unconverted substrate that remained in solution was inspected via NMR for the presence of deuterium. This would occur if there was exchange at the α-C or β-C, presumably via a transfer hydrogenation-like mechanism, before the desired HDO. Such exchange would reflect the reactive gas or, if activated hydrogen on the catalyst surface exchanged rapidly with the solvent, the exchange would reflect the solvent isotopes and these must be accounted for in any sound mechanistic study. There were no signals for deuterium in

unconverted 1,2-PD under the conditions of permutation **A**. However, permutation **B** revealed 12% D incorporation at the α-C and 3% D incorporation at the β-C after 4 hours, i.e. the exchanged isotope came from the solvent, not the reactive gas, itself. While the extent of exchange was rather small, it does suggest the activated hydrogen bound to the catalyst readily exchanged with the water solvent. Enlarged NMR spectra of the α-C and β-C of 1,2-PD can be found in Appendix B.

As mentioned in the previous section, isotopic exchange between the gas and solvent can obscure results obtained from a deuterium incorporation study, especially if the reaction mechanism involves the solvent. This phenomenon was first investigated by subjecting the solvent, water, to the same reaction conditions with D_2 gas in the absence of substrate and catalyst for 4 hours. This resulted in a very small peak seen for partially deuterated water, DHO, in ^2H NMR where it was quantified using DMSO-d_6 as an internal standard (see Appendix B). Next, the previous experiment was augmented by the addition of the catalyst, Pt-WO_x/TiO_2, into the solvent. This resulted in significantly more deuteria detected within the solvent. The results are seen in Table 3.5 below.

Table 3.5: Concentration of partially deuterated water (DHO) in the resulting solution of isotope exchange between D_2 gas and water with and without the catalyst.

Reaction system	Concentration of DHO (mol L^{-1})
Without catalyst [a]	1
With catalyst [b]	12

[a] 1 mL of solution (water) in a pressure reactor at 180 °C under 70 bar D_2. [b] Same experiment except with the addition of 50 mg Pt-WO_x/TiO_2.

For the analysis, only partially deuterated water, DHO, was considered the product rather than D_2O under the assumption that a molecule of water only exchanges once. It is seen that the isotope exchange is much greater in the presence of the catalyst indicating the catalyst is facilitating the exchange between the gas and solvent.

To further study the degree of isotope exchange and implications on data analysis of deuterium incorporation, hydrogenation of TEGDA was carried out. TEGDA was utilized for its water-solubility and to observe deuterium incorporation in a mechanistically simpler reduction, known to occur over Pt sites alone.[54] Scheme 3.3 shows expected deuterium incorporation into the alkene after hydrogenation with permutation **A**. Pt sites should activate D_2 gas and saturate the double bond giving a deuterium on each carbon.

Scheme 3.3: Expected deuterium placement after incorporation in D_2/H_2O system over Pt-WO_x/TiO_2 for the hydrogenation of TEGDA.

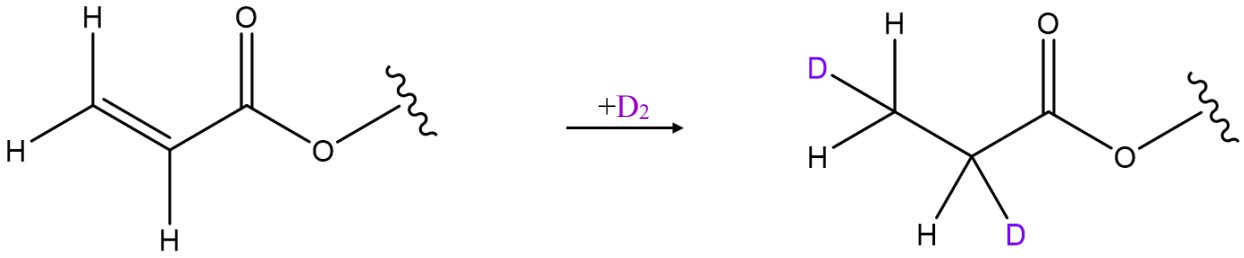

Reaction permutations **A** and **B** were conducted with TEGDA as the substrate (5 wt% TEGDA in H_2O, 20 mL) in the stirred tank reactor at 25 °C under 50 bar of reactive gas pressure with 0.1 g Pt-WO_x/TiO_2. A lower temperature was used due to the facility of alkene hydrogenation over Pt. After reaction, the product solution was analyzed with ^{13}C NMR and the relative amounts of isotopologues were quantified. The NMR spectral region for the α-C of TEGDA after reaction under conditions of permutation **B** is shown in Figure 3.6.

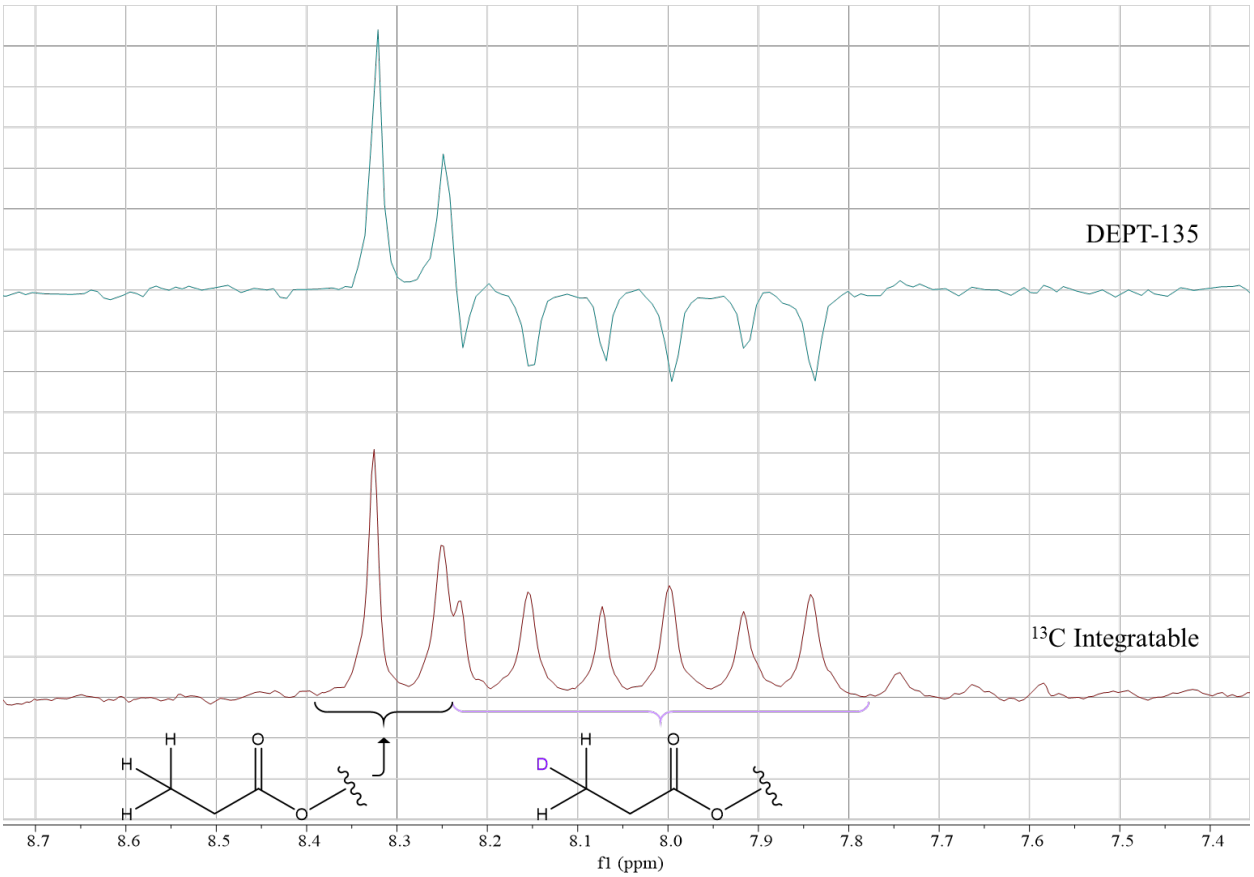

Figure 3.6: NMR analysis on the α-C of TEGDA after hydrogenation with the H_2/D_2O reaction system.

Again, all peaks were individually fit with a Gaussian integral, so the two peaks overlapping at ~8.25 ppm are properly quantified. There are two singlets that correspond to a α-C with only H atoms and two sets of triplets that correspond to a α-C with a bonded D atom. The reason for each compound showing two sets of each signal was explained in Section 3.3.1. Quantitative results from experiments using systems **A** and **B** are shown in Table 3.6.

Table 3.6: Results of deuterium incorporation reactions of TEGDA hydrogenation.[a]

Reaction system (gas/solvent)	α-C		β-C	
	$-CH_3-$	$-CH_2D-$	$-CH_2-$	-CHD-
D_2/H_2O (**A**)	73%	27%	85%	15%
H_2/D_2O (**B**)	40%	60%	48%	52%

[a] Reactions were performed with 20 mL of aqueous substrate solution (5 wt% TEGDA) in the stirred tank reactor at 25 °C under 50 bars of reactive gas with 0.1 g Pt-WO_x/TiO_2 and 2 h reaction time.

The data show that in all cases over half of the deuterons (or protons) incorporated via hydrogenation are derived from the solvent. The simplicity of this reaction precludes consideration of tungsten involvement in the reaction and demonstrates that even at mild temperatures there is isotope exchange occurring at the surface of the catalyst, consistent with early studies.[55-56] This exchange is expected to be between activated deuterium (or hydrogen) and water (or D_2O). It was determined by NMR that the reaction reached full conversion in less than 2 hours which is significantly faster than the HDO reaction (see Section 3.5). Notably HDO occurs at higher temperatures than olefin hydrogenation. Comparing the CH_3 species in permutation **A** with the CH_2D species of permutation **B** at the α-C, less isotope incorporation occurred from the solvent when the solvent was D_2O versus H_2O. The same pattern was seen at the β-C. This is consistent with kinetic isotope theory that breaking the bonds of D_2O should be slower than for H_2O. Additionally, it has been reported the rate of adsorption of hydrogen on Pt metal exceeds that of deuterium by about 1.5.[57]

It may be concluded that isotope exchange between surface activated hydrogen and the water solvent occurs much faster than the HDO reaction, since significant deuterium incorporation was observed in TEGDA hydrogenation with H_2/D_2O even at a much lower temperature than HDO reaction temperatures. In spite of this rapid exchange at the surface, a relatively low rate of isotope

exchange into the 1,2-PD substrate was observed (≤12% in 4 hours), presumably occurring via a transfer hydrogenation type mechanism. Accordingly, isotope incorporation during HDO should occur primarily through the desired reduction reactions, and the 100% isotope incorporation seen on the α-C does not occur from background exchange over the catalyst surface and is inconsistent with the RMvK mechanism.

An enol intermediate is consistent with the observed isotope incorporation pattern. Since the Pt surface sites contain the hydrogen isotope of the solvent, hydrogenation of the enol would install that isotope on both the α-C and the β-C positions. It should be noted that tautomerization of the enol to an aldehyde followed by reduction would give the same isotope incorporation. The labeling of the β-C under permutation **B** is not quantitative (81%) and may be explained by partial competition from formation of an oxocarbenium ion via intramolecular hydride shift as suggested by Dumesic and coworkers.[38] While kinetically competing, we conclude the oxocarbenium is not dominant compared to the enol and only contributes the minor labeling product (19%), **1**.

3.4 Mass Transfer Limitations

Before any kinetic analyses are done for a reaction, the system must first be verified to be free of mass transfer limitations. This system is defined as a three-phase, slurry, batch reactor. The presence of any mass transfer limitations, gas-liquid, liquid-solid, or intraparticle, would inhibit measurement of the intrinsic kinetics of the reaction, and any data obtained would be clouded by the effects of mass transfer resistances throughout the reactor volume. Criteria were used from Ramachandran and Chaudhari[58] to analyze each regime of mass transfer, they are

$$\alpha_1 = \frac{R_A}{k_L \cdot a_B \cdot A^*} < 0.1 \quad (1)$$

$$\alpha_2 = \frac{R_A}{k_s \cdot a_p \cdot A^*} < 0.1 \quad (2)$$

$$\phi_{exp} = \frac{d_p}{6}\left(\frac{\rho_p \cdot R_A}{w \cdot D_{eA} \cdot A^*}\right)^{0.5} < 0.2 \quad (3)$$

Equations 1-3 represent the gas-liquid, liquid-solid, and intraparticle regimes, respectively. They are expressed as the observed rate of the HDO reaction of 1,2-PD over the maximum possible rates of mass transfer, and if each requirement is met, it can be said that the system is not mass transfer limited. This method has been used previously in literature.[59]

The reaction rate, R_A, was found by initial rates of 1,2-PD HDO outlined in Section 3.5 and is converted to appropriate units to give 0.0362 mol L^{-1} h^{-1}. Chaudhari and coworkers[60] provide an experimental correlation to calculate k_La_B for autoclave reactors shown in Equation 4 below:

$$k_L a_B = 1.48x10^{-3}(N)^{2.18}\left(\frac{V_g}{V_L}\right)^{1.88}\left(\frac{d_I}{d_T}\right)^{2.16}\left(\frac{h_1}{h_2}\right)^{1.16} \quad (4)$$

The values used here are as follows: N, the stirring speed, is 16.7 Hz, the volume of the gas and liquid, V_g and V_L, respectively are both 2.5 x 10^{-5} m^3 since 25 mL of reaction solution is used in a 50 mL vessel, the diameter of the impeller, d_I, is 0.02053 m, the diameter of the reactor tank, d_T, is 0.03278 m, height of the impeller from the bottom of the tank, h_1, is 0.0125 m, and the height of the liquid in the tank, h_2, is 0.0284 m. This yields a k_La_B value of 0.096 s^{-1}. The concentration of hydrogen gas at the gas-liquid interface, A^*, was assumed to be the equilibrium solubility of hydrogen in water at reaction conditions. Solubility data of hydrogen was used from the dissertation of Suciu[61] which is tabulated in IUPAC Solubility Data Series by Young.[62] A value of hydrogen solubility in water was interpolated between data points of 34 bar and 69 bar at ~178 °C

since hydrogen solubility in water has been shown to have a linear relationship with pressure.[63] The value used for A^* is 0.0536 kmol m^{-3}. Applying these parameters in Equation 1 gives an α_1 of 0.002 which is well below 0.1 indicating the system is not limited by the rate of gas to liquid mass transfer.

The criteria for the liquid-solid regime in Equation 2 was evaluated. The liquid-solid mass transfer coefficient, k_s, was calculated through a dimensionless correlation of the Sherwood number done by Sano et al.,[64] Equation 5:

$$Sh = \left[2 + 0.4\left(\frac{\varepsilon \cdot d_p^4}{\nu^3}\right)^{\frac{1}{4}} Sc^{\frac{1}{3}}\right] \cdot \phi_c \tag{5}$$

The Sherwood number (Sh) is defined as

$$Sh = \frac{k_s \cdot d_p}{D_A} \tag{6}$$

where d_p is the specific surface diameter and D_A is the diffusivity of hydrogen gas in water. Experimental data for D_A is provided by Cussler[65] and is 4.50 x 10^{-9} m^2 s^{-1}. The particle diameter, d_p, is defined in Equation 7.[64]

$$d_p = \frac{6}{\rho_p \cdot S_w} \tag{7}$$

The density of the solid (ρ_s) and specific surface area (S_w) are assumed to be equal to that of pure TiO_2 where a range was obtained from Evonik and averaged (ρ_s = 1.4 x 10^5 g m^{-3} and S_w = 50 m^2 g^{-1}).[66] This gave a value for d_p of 8.57 x 10^{-7} m. For the kinematic viscosity of water, v, in Equation 5, a value of 2.94 x 10^{-7} m^2 s^{-1} at 100 °C will be used[67] which is a limiting case since the kinematic viscosity of water decreases as temperature increases, therefore, increasing the rate of mass transfer. The Schmidt number (Sc) is defined as

$$Sc = \frac{\nu}{D_A} \tag{8}$$

Sc was calculated to be 65.3. Next, the rate of flow energy supply per unit mass of liquid, ε, is calculated to be 675 $m^2\ s^{-3}$ by Equation 9 which utilizes a power number, N_p, of 4 found in the work of Bates et al.[68]

$$\varepsilon = \frac{N_p \cdot l^5 \cdot n^3}{V_L} \tag{9}$$

The variable l is the diameter of impeller, n is the rps of impeller, in rad s^{-1}, and V_L is the volume of liquid. Finally, Carman's surface factor, ϕ_c, from Equation 5 is defined as

$$\phi_c = \frac{6}{\rho_p \cdot S_w \cdot d_p'} \tag{10}$$

where d_p' is the screen diameter taken as 2 x d_p based on a graphical approximation in the work of Sano et al.[64] Equation 11 gives $\phi_c = 0.5$. Combining Equations 5 and 6 and rearranging for k_s gives a value for the liquid-solid mass transfer coefficient of 6.71 x 10^{-3} m s^{-1}. From Equation 2, a_p is the external surface area of the catalyst per unit volume of reactor and is calculated to be 2.0 x 10^6 $m^2\ m^{-3}$. Using these values obtained and plugging into Equation 2 yields an α_2 of 1 x 10^{-8} which is orders of magnitude below 0.1 indicating the system is not mass transfer limited in the liquid-solid regime.

Finally, intraparticle mass transfer was investigated. Most of the variables in Equation 3 have already been found. The term *w*, the weight of catalyst loading per unit volume of the reactor, comes out to be 40 kg m^{-3}. The effective diffusivity of hydrogen within the pores of the catalyst, D_{eA}, is determined by Equation 11:

$$D_{eA} = \frac{P \cdot D_A}{\tau} \quad (11)$$

where P is the porosity of the catalyst particles and τ is the tortuosity factor, both assumed to be 0.6 and 3.0, respectively.[59] These assumptions are taken from a previous work that used powdered catalysts in a slurry, batch reactor.[59] The value obtained for D_{eA} is 9.0 x 10^{-10} m^2 s^{-1}. Calculating ϕ_{exp} from Equation 3 gives a value of 1 x 10^{-4}. This is significantly below the criteria of 0.2, so it is accurate to say there is no presence of intraparticle mass transfer limitations.

3.5 Kinetic Isotope Effect

To further explore the HDO reaction pathway of this alcohol over the Pt-WO_x/TiO_2 catalyst, a KIE study was carried out. This allowed insight into the rate-determining step of the reaction based on a ratio of the rate constants of two systems differing only by isotope incorporation. Isotopically labeled substrates have been used to observe a KIE in HDO reactions[44] and deuterium gas used to be incorporated into products,[45] but to the best of our knowledge observing a KIE with deuterium gas or D_2O has not been performed for HDO reactions involving linear alcohols. In this section, two reaction systems were compared: a system using H_2 as the gas and H_2O as the solvent, and a system using D_2 as the gas and D_2O as the solvent. These systems were chosen due to the rapid exchange between the gas and solvent in the presence of the catalyst (cf. Section 3.3.2). Since the H/D exchange is so facile, experiments using different isotopes in the gas versus solvent would not be conclusive because of the uncertainty to whether an H or D atom was involved in the rate-determining step. A KIE is defined as the rate constant of the reaction for the lighter isotopic system over the rate constant of the reaction for the heavier isotopic system, k_H/k_D.

Reactions were performed in a stirred tank reactor equipped with a sampling port using 5 wt% 1,2-PD in H_2O (25 mL), 50 bar H_2 at 180 °C over 1.0 g Pt -WO_x/TiO_2 and a 4 hour reaction time, Figure 3.7. As the reaction proceeds, selectivity to pentanol decreases. This was expected since the pentanol produced would have more opportunity to be further deoxygenated over the catalyst to form pentane, although this species was not calibrated for detection in GC analyses due to insolubility. A decrease in the conversion rate was seen after 1.5 hours. It is unclear why the

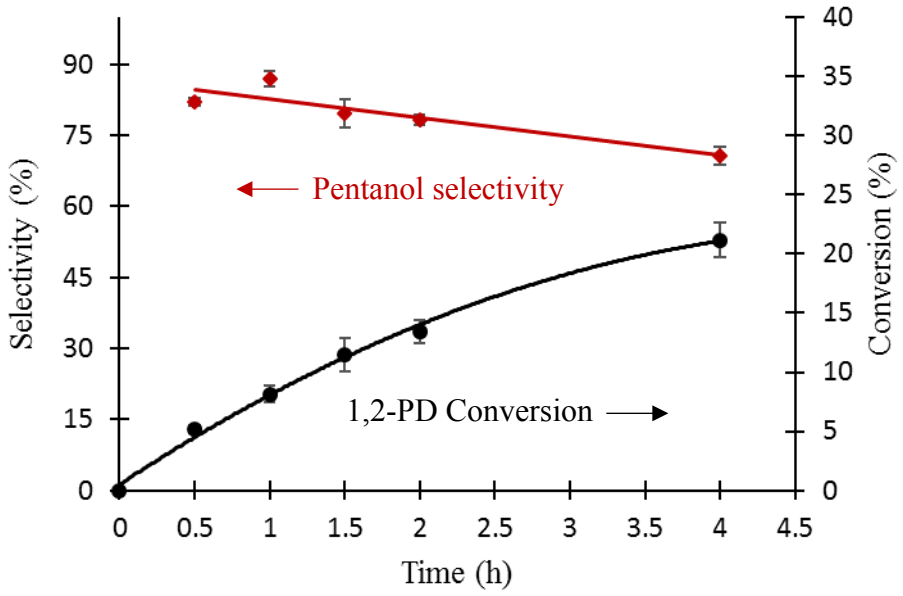

Figure 3.7: Selectivity and conversion as a function of time for the HDO of 1,2-PD in a batch stirred tank reactor with the substrate solution (5 wt% 1,2-PD in H_2O, 25 mL) under 50 bars H_2 at 180 °C over 1.0 g Pt-WO_x/TiO_2.

conversion rate decreased after this time; a form of catalyst deactivation is the most likely cause. However, this issue is disregarded since the relevant data is contained within 15% conversion, and this region does not show a significant decrease in conversion rate.

Conversion data of both systems used for kinetic analysis, H_2/H_2O and D_2/D_2O exhibit first-order kinetics during initial rates as a plot of the natural logarithm of PD concentration as a function of time produces a linear plot (Figure 3.8). The plots in Figure 3.8 display a very good trend in the data points up to 1.5 h for both systems, so the first four points of each set were used

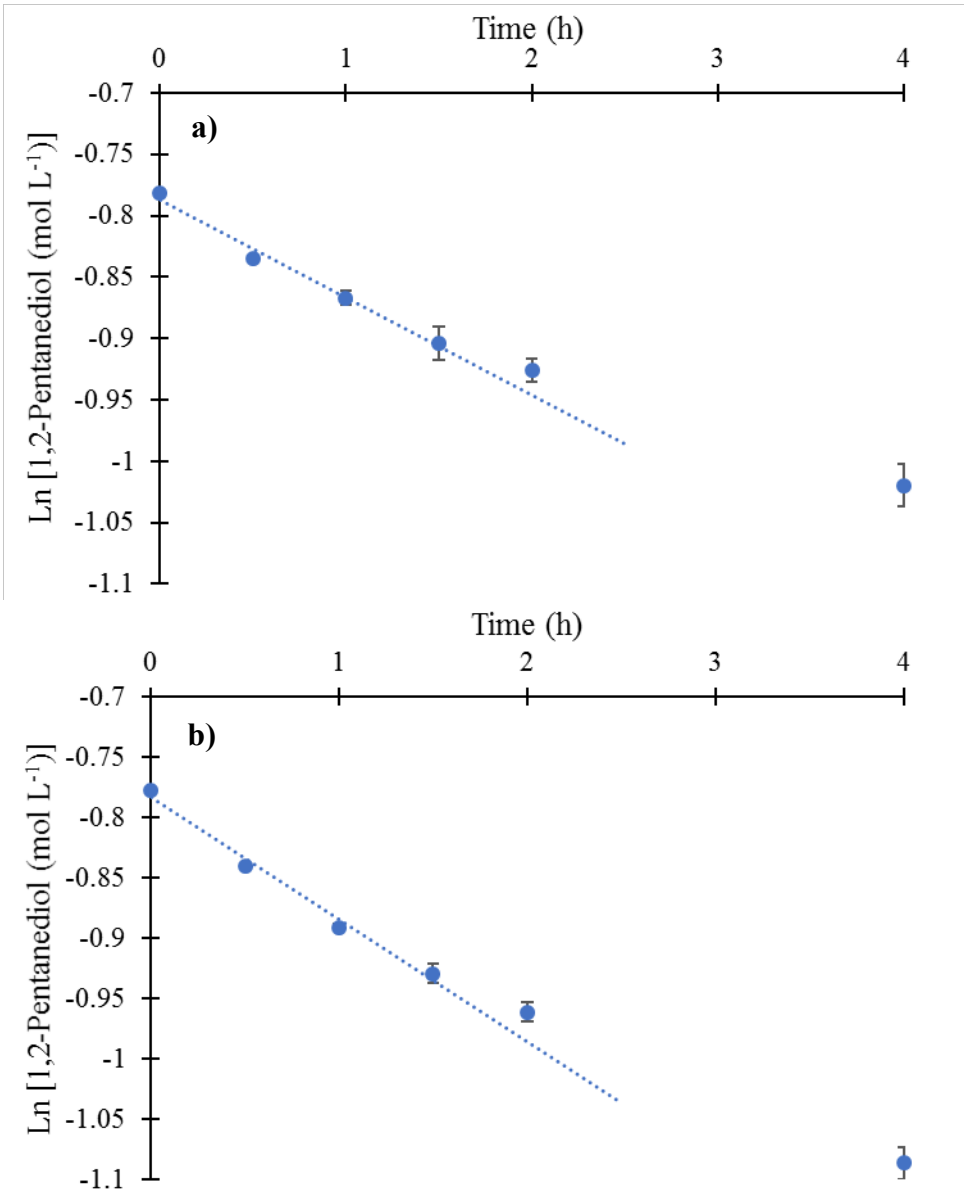

Figure 3.8: Natural logarithm of 1,2-PD concentration as a function of time for the HDO of 1,2-PD in a stirred tank reactor with **a)** the substrate solution (5 wt% PD in H_2O, 25 mL) under 50 bars H_2 at 180 °C over 1.0 g Pt-WO_x/TiO_2 and **b)** the substrate solution (5 wt% 1,2-PD in D_2O, 25 mL) under 50 bars D_2 at 180 °C over 1.0 g Pt-WO_x/TiO_2.

in the rate calculations. The data points were fitted with a trendline, and the slope of this trendline was taken to be equal to the rate constant, k, of the reaction since the kinetics can be considered pseudo-first order. Also, an observed reaction rate was found by the slope of 1,2-PD concentration as a function of time and converted into the units of mmol 1,2-PD g-catalyst^{-1} h^{-1}. The standard error of the mean was calculated for each value, and the equations involving these calculations can be found in Appendix G. Table 3.7 displays results of these calculations.

Table 3.7: Rate data assuming first order kinetics for reactions performed in a stirred tank reactor with the substrate solution (5 wt% 1,2-PD in solvent, 25 mL) under 50 bars reactive gas at 180 °C over 1.0 g Pt-WO_x/TiO_2.

Reaction System (gas/solvent)	Observed Rate (mmol 1,2-PD g-cat.$^{-1}$ h^{-1})	k_x[a] (h^{-1})
H_2/H_2O	0.90 ± 0.08	0.085 ± 0.007
D_2/D_2O	1.06 ± 0.05	0.101 ± 0.005

[a] The term k_x is defined as k_H for the H_2/H_2O system and as k_D for the D_2/D_2O system.

In this system, a primary KIE would arise if the rate-determining step involved the cleavage or formation of a hydrogen covalent bond. This effect can give values for k_H/k_D on the order of 10 or higher depending on the reaction.[69] A secondary KIE is seen not when the rate determining step involves breaking or forming of bonds with H or D, but when these species are present in the α or β position from the reaction center affecting the zero-point energy of ordinary vibration. This effect is normally around 1.15 to 1.25 for reactions involving, but not limited to, sp^3 to sp^2 conversions.[70] In addition, a $k_H/k_D < 1.0$ signifies an inverse KIE where the mechanism often involves a transformation from sp^2 to sp^3.[71]

For this system, a k_H/k_D value of 0.84 ± 0.11 was observed between the undeuterated and deuterated gas/solvent systems. Clearly no primary KIE exists in this system and the rate-determining step does not involve the gas nor the solvent. Accordingly, the direct C–O scission mechanism can be eliminated, since the mechanism involves a hydride species breaking its bond with Pt and forming a bond with the substrate. While the k_H/k_D value suggests an inverse KIE, the uncertainty in the measurement precludes a strong conclusion, except to note the absence of a primary KIE. Although the KIE study does not affirmatively support which mechanism is taking place, conclusive evidence of disproof of direct C–O scission is nonetheless invaluable.[72]

Chapter 4: Conclusions and Recommendations

4.1 Conclusions

The studies conducted in this thesis have elucidated the aqueous HDO reaction mechanism of 1,2,6-HT over a Pt-WO_x/TiO_2 catalyst, by reference to a model compound, 1,2-PD. The absence of a primary kinetic isotope effect using D_2/D_2O versus H_2/H_2O disproves the possible direct C–O scission mechanism. Deuterium incorporation using two different reaction systems, D_2/H_2O and H_2/D_2O, showed a significant incorporation of isotopes from the solvent rather than the gas in the reaction product. The incorporation seen in both the α-C and β-C did not initially support any of the proposed mechanisms. Rather, rapid and facile isotope exchange between the surface of the catalyst and the water solvent was observed. This was confirmed by measuring deuterium incorporation during an alkene hydrogenation, a reaction with lower activation energy, faster rate and a simpler mechanism than HDO. In this case, the isotope incorporated into the product primarily came from the solvent. Given that water / surface isotope exchange was much faster than the HDO reaction, the observed product isotope distributions provide additional insight into the mechanism. Nearly equal deuterium incorporation in the α-C and β-C support the preferred intermediacy of an enol formed by acid-site-catalyzed dehydration of the secondary hydroxyl. The intermediacy of an oxocarbenium in the alpha position formed by intramolecular hydride transfer[38] may be competitive but the enol dominates. Further, the reverse Mars-van Krevelen mechanism is not consistent with the observed isotope incorporation since this mechanism should not provide the observed pattern of nearly equal isotope incorporation at the α-C and β-C. Accordingly, a logical mechanism for HDO of 1,2,6-HT comprises the following steps:

1. Acid catalyzed dehydration of the secondary hydroxyl by Brønsted sites of the metal oxide forming a secondary carbenium ion.
2. Subsequent proton abstraction from the α-C by water forming an enol intermediate.
3. Hydrogenation of the double bond of the enol over Pt metal followed by desorption yielding 1,6-HD.

Regeneration of the acid sites would follow the mechanism described by Huber and coworkers, which explains the preferred behavior of TiO_2 as a support.[23]

i. Hydrogen molecules are activated by Pt.

ii. Hydrogen moves from the Pt-TiO_2 interface to WO_x sites via spillover.[40]

iii. The hydrogen atoms exist in the form of H^+ and e^- pairs and reduce W=O species to W–OH Brønsted sites with tungsten in the 5+ oxidation state.

To the best of our knowledge, the methods used in this study are unprecedented for investigating the mechanism of HDO over supported metal-metal oxide catalysts. This provides a new perspective of the proposed reaction mechanisms of this system. The mechanism may extend to a broad range of linear polyols over supported metal-metal oxide catalysts, which have shown the best performance for deoxygenation of certain feedstocks derived from biomass.[29] Understanding the reaction mechanism is essential for optimizing catalyst design,[20] so the findings here further advanced technologies for the utilization of sustainable feedstocks.

4.2 Recommendations

In this study it was seen how the presence of the catalyst affected isotope exchange between the gas and liquid phases. It is expected that various catalysts will have different exchange rates depending on the reducible metal's affinity for hydrogen/deuterium activation, metal oxide acidity, and support reducibility. All of these parameters can be systematically tested and material property relationships to isotope exchange deduced. This would possibly impact mechanistic studies using deuterium incorporation and KIE methods that employ heterogeneous catalysts for reactions involving hydrogen/deuterium gas and polar protic solvents.

Inspection of solvent effects could be another valuable avenue of research. Utilization of aprotic solvents and their effects on the rate of reaction or deuterium incorporation is expected to be insightful. Also, this may decrease the amount of isotopic exchange between the gas and solvent. Protic solvents other than water may also provide interesting results possibly based on the pK_a value of the solvent. Interaction between the catalyst, specifically the Brønsted acid sites of the metal oxide, and the solvent is another aspect where the system could be affected.

In addition, a techno-economic assessment can be done for a process involving the production of 1,6-HD from an appropriate biomass-derived intermediate, not necessarily 1,2,6-HT, with the present catalyst. Just like any other technology, the valorization of sustainable feedstocks such as biomass involves economic feasibility. It should be recognized that aqueous conditions in the presence of alcohols can lead to challenging, energy-intensive separations, which would increase the cost of production.

References

1. Jill, J.; Juan, M.; Anwar, A.; Adam, M.; R., S. D., Kinetic characterization of biomass dilute sulfuric acid hydrolysis: Mixtures of hardwoods, softwood, and switchgrass. *AIChE Journal* **2008,** *54* (6), 1637-1645.

2. Sharma, A.; Pareek, V.; Zhang, D., Biomass pyrolysis—A review of modelling, process parameters and catalytic studies. *Renewable and Sustainable Energy Reviews* **2015,** *50*, 1081-1096.

3. K., P. K., A study of chemical structure of soft and hardwood and wood polymers by FTIR spectroscopy. *Journal of Applied Polymer Science* **1999,** *71* (12), 1969-1975.

4. Bajpai, P., Structure of Lignocellulosic Biomass. In *Pretreatment of Lignocellulosic Biomass for Biofuel Production*, Springer Singapore: Singapore, 2016; pp 7-12.

5. Yang, H.; Yan, R.; Chen, H.; Lee, D. H.; Zheng, C., Characteristics of hemicellulose, cellulose and lignin pyrolysis. *Fuel* **2007,** *86* (12), 1781-1788.

6. O'Sullivan, A. C., Cellulose: the structure slowly unravels. *Cellulose* **1997,** *4* (3), 173-207.

7. Payen, A., Sur un moyen d'isoler le tissue élémentaire des bois. *CR Hebd. Seances Acad. Sci* **1838,** *7*, 1125.

8. Marchessault, R. H.; Sundararajan, P. R., 2 - Cellulose A2 - ASPINALL, GERALD O. In *The Polysaccharides*, Academic Press: 1983; pp 11-95.

9. Sjöström, E.; Alén, R., *Analytical methods in wood chemistry, pulping, and papermaking*. Springer Science & Business Media: 2013.

10. Sjöström, E., The structure of wood. *Wood chemistry: fundamentals and applications.* **1981**, 1-20.

11. Alonso, D. M.; Wettstein, S. G.; Dumesic, J. A., Bimetallic catalysts for upgrading of biomass to fuels and chemicals. *Chemical Society Reviews* **2012,** *41* (24), 8075-8098.

12. Cheng, J., *Biomass to renewable energy processes*. 2 ed.; CRC press: 2017.

13. Mosier, N.; Wyman, C.; Dale, B.; Elander, R.; Lee, Y. Y.; Holtzapple, M.; Ladisch, M., Features of promising technologies for pretreatment of lignocellulosic biomass. *Bioresource Technology* **2005,** *96* (6), 673-686.

14. Aspinall, G. O., 12 - Chemistry of Cell Wall Polysaccharides A2 - Preiss, Jack. In *Carbohydrates: Structure and Function*, Academic Press: 1980; pp 473-500.

15. Saha, B. C., Hemicellulose bioconversion. *Journal of Industrial Microbiology and Biotechnology* **2003,** *30* (5), 279-291.

16. Singh, M. A.; Jong‐Min, L.; Yeong‐Cheol, K.; Taek, H. I.; No‐Joong, P.; Kyu, H. Y.; Jong‐San, C.; Jin‐Soo, H., Furfural: Hemicellulose/xylosederived biochemical. *Biofuels, Bioproducts and Biorefining* **2008,** *2* (5), 438-454.

17. Jean‐Paul, L.; Evert, v. d. H.; Jeroen, v. B.; Richard, P., Furfural—A Promising Platform for Lignocellulosic Biofuels. *ChemSusChem* **2012,** *5* (1), 150-166.

18. Hutchings, G. J., Heterogeneous catalysts—discovery and design. *Journal of Materials Chemistry* **2009,** *19* (9), 1222-1235.

19. Friend, C. M.; Xu, B., Heterogeneous Catalysis: A Central Science for a Sustainable Future. *Accounts of Chemical Research* **2017,** *50* (3), 517-521.

20. Walker, T. W.; Motagamwala, A. H.; Dumesic, J. A.; Huber, G. W., Fundamental catalytic challenges to design improved biomass conversion technologies. *Journal of Catalysis* **2019,** *369*, 518-525.

21. Buntara, T.; Noel, S.; Phua, P. H.; Melián-Cabrera, I.; de Vries, J. G.; Heeres, H. J., From 5-Hydroxymethylfurfural (HMF) to Polymer Precursors: Catalyst Screening Studies on the Conversion of 1,2,6-hexanetriol to 1,6-hexanediol. *Topics in Catalysis* **2012,** *55* (7), 612-619.

22. Allgeier, A. M.; De Silva, W. I. N.; Menning, C. A.; Ritter, J. C.; Sengupta, S. K. Production of alpha, omega-diols. US9018423, April 28, 2015, 2014.

23. He, J.; Burt, S. P.; Ball, M.; Zhao, D.; Hermans, I.; Dumesic, J. A.; Huber, G. W., Synthesis of 1,6-Hexanediol from Cellulose Derived Tetrahydrofuran-Dimethanol with Pt-WOx/TiO2 Catalysts. *ACS Catalysis* **2018,** *8* (2), 1427-1439.

24. Figueiredo, F. C. A.; Jordão, E.; Carvalho, W. A., Adipic ester hydrogenation catalyzed by platinum supported in alumina, titania and pillared clays. *Applied Catalysis A: General* **2008,** *351* (2), 259-266.

25. Lligadas, G.; Ronda, J. C.; Galià, M.; Cádiz, V., Plant Oils as Platform Chemicals for Polyurethane Synthesis: Current State-of-the-Art. *Biomacromolecules* **2010,** *11* (11), 2825-2835.

26. Xie, J.; Falcone, D. D.; Davis, R. J., Restructuring of supported PtSn bimetallic catalysts during aqueous phase oxidation of 1,6-hexanediol. *Journal of Catalysis* **2015,** *332*, 38-50.

27. Rose, M.; Palkovits, R., Isosorbide as a Renewable Platform chemical for Versatile Applications—Quo Vadis? *ChemSusChem* **2012,** *5* (1), 167-176.

28. Wang, T.; Nolte, M. W.; Shanks, B. H., Catalytic dehydration of C6 carbohydrates for the production of hydroxymethylfurfural (HMF) as a versatile platform chemical. *Green Chemistry* **2014,** *16* (2), 548-572.

29. Tomishige, K.; Nakagawa, Y.; Tamura, M., Selective hydrogenolysis and hydrogenation using metal catalysts directly modified with metal oxide species. *Green Chemistry* **2017,** *19* (13), 2876-2924.

30. Nakagawa, Y.; Ning, X.; Amada, Y.; Tomishige, K., Solid acid co-catalyst for the hydrogenolysis of glycerol to 1,3-propanediol over Ir-ReOx/SiO2. *Applied Catalysis A: General* **2012,** *433-434*, 128-134.

31. Xiao, B.; Zheng, M.; Li, X.; Pang, J.; Sun, R.; Wang, H.; Pang, X.; Wang, A.; Wang, X.; Zhang, T., Synthesis of 1,6-hexanediol from HMF over double-layered catalysts of Pd/SiO2 + Ir-ReOx/SiO2 in a fixed-bed reactor. *Green Chemistry* **2016,** *18* (7), 2175-2184.

32. Zhou, W.; Luo, J.; Wang, Y.; Liu, J.; Zhao, Y.; Wang, S.; Ma, X., WOx domain size, acid properties and mechanistic aspects of glycerol hydrogenolysis over Pt/WOx/ZrO2. *Applied Catalysis B: Environmental* **2019,** *242*, 410-421.

33. Boffa, A. B.; Lin, C.; Bell, A. T.; Somorjai, G. A., Lewis acidity as an explanation for oxide promotion of metals: implications of its importance and limits for catalytic reactions. *Catalysis Letters* **1994,** *27* (3), 243-249.

34. Johnson, G. R.; Bell, A. T., Effects of Lewis acidity of metal oxide promoters on the activity and selectivity of Co-based Fischer–Tropsch synthesis catalysts. *Journal of Catalysis* **2016,** *338*, 250-264.

35. Mironenko, A. V.; Vlachos, D. G., Conjugation-Driven "Reverse Mars–van Krevelen"-Type Radical Mechanism for Low-Temperature C–O Bond Activation. *Journal of the American Chemical Society* **2016,** *138* (26), 8104-8113.

36. Goulas, K. A.; Mironenko, A. V.; Jenness, G. R.; Mazal, T.; Vlachos, D. G., Fundamentals of C–O bond activation on metal oxide catalysts. *Nature Catalysis* **2019,** *2* (3), 269-276.

37. Koso, S.; Nakagawa, Y.; Tomishige, K., Mechanism of the hydrogenolysis of ethers over silica-supported rhodium catalyst modified with rhenium oxide. *Journal of Catalysis* **2011,** *280* (2), 221-229.

38. Chia, M.; Pagán-Torres, Y. J.; Hibbitts, D.; Tan, Q.; Pham, H. N.; Datye, A. K.; Neurock, M.; Davis, R. J.; Dumesic, J. A., Selective Hydrogenolysis of Polyols and Cyclic Ethers over Bifunctional Surface Sites on Rhodium–Rhenium Catalysts. *Journal of the American Chemical Society* **2011,** *133* (32), 12675-12689.

39. Prasomsri, T.; Nimmanwudipong, T.; Roman-Leshkov, Y., Effective hydrodeoxygenation of biomass-derived oxygenates into unsaturated hydrocarbons by MoO3 using low H2 pressures. *Energy & Environmental Science* **2013,** *6* (6), 1732-1738.

40. Karim, W.; Spreafico, C.; Kleibert, A.; Gobrecht, J.; VandeVondele, J.; Ekinci, Y.; van Bokhoven, J. A., Catalyst support effects on hydrogen spillover. *Nature* **2017,** *541*, 68.

41. Prins, R., Hydrogen Spillover. Facts and Fiction. *Chemical Reviews* **2012,** *112* (5), 2714-2738.

42. Wawrzetz, A.; Peng, B.; Hrabar, A.; Jentys, A.; Lemonidou, A. A.; Lercher, J. A., Towards understanding the bifunctional hydrodeoxygenation and aqueous phase reforming of glycerol. *Journal of Catalysis* **2010,** *269* (2), 411-420.

43. Nolan, M. R.; Sun, G.; Shanks, B. H., On the selective acid-catalysed dehydration of 1,2,6-hexanetriol. *Catalysis Science & Technology* **2014,** *4* (8), 2260-2266.

44. Lugo-José, Y. K.; Behtash, S.; Nicholson, M.; Monnier, J. R.; Heyden, A.; Williams, C. T., Unraveling the mechanism of propanoic acid hydrodeoxygenation on palladium using deuterium kinetic isotope effects. *Journal of Molecular Catalysis A: Chemical* **2015,** *406*, 85-93.

45. Ben, H.; Ferguson, G. A.; Mu, W.; Pu, Y.; Huang, F.; Jarvis, M.; Biddy, M.; Deng, Y.; Ragauskas, A. J., Hydrodeoxygenation by deuterium gas - a powerful way to provide insight into the reaction mechanisms. *Physical Chemistry Chemical Physics* **2013,** *15* (44), 19138-19142.

46. Van Nordstrand, R. A.; Lincoln, A. J.; Carnevale, A., Determination of Metallic Platinum-Alumina Catalysts by X-Ray Diffraction. *Analytical Chemistry* **1964,** *36* (4), 819-824.

47. Nguyen, V.-L.; Ohtaki, M.; Ngo, V. N.; Cao, M.-T.; Nogami, M., Structure and morphology of platinum nanoparticles with critical new issues of low- and high-index facets. *Advances in Natural Sciences: Nanoscience and Nanotechnology* **2012,** *3* (2), 025005.

48. Iddir, H.; Skavysh, V.; Öğüt, S.; Browning, N. D.; Disko, M. M., Preferential growth of Pt on rutile TiO2. *Physical Review B* **2006,** *73* (4), 041403.

49. Wang, C.; Lee, J. D.; Ji, Y.; Onn, T. M.; Luo, J.; Murray, C. B.; Gorte, R. J., A Study of Tetrahydrofurfuryl Alcohol to 1,5-Pentanediol Over Pt–WOx/C. *Catalysis Letters* **2018,** *148* (4), 1047-1054.

50. Nelson, R. C.; Baek, B.; Ruiz, P.; Goundie, B.; Brooks, A.; Wheeler, M. C.; Frederick, B. G.; Grabow, L. C.; Austin, R. N., Experimental and Theoretical Insights into the Hydrogen-Efficient Direct Hydrodeoxygenation Mechanism of Phenol over Ru/TiO2. *ACS Catalysis* **2015,** *5* (11), 6509-6523.

51. Riegel, S. D.; Leskowitz, G. M., Benchtop NMR spectrometers in academic teaching. *TrAC Trends in Analytical Chemistry* **2016,** *83*, 27-38.

52. Darwish, T. A.; Yepuri, N. R.; Holden, P. J.; James, M., Quantitative analysis of deuterium using the isotopic effect on quaternary 13C NMR chemical shifts. *Analytica Chimica Acta* **2016,** *927*, 89-98.

53. Butler, J. P.; Rolston, J. H.; Stevens, W. H., Novel Catalysts for Isotopic Exchange between Hydrogen and Liquid Water. In *Separation of Hydrogen Isotopes*, AMERICAN CHEMICAL SOCIETY: 1978; Vol. 68, pp 93-109.

54. Rylander, P., *Catalytic hydrogenation over platinum metals*. Academic Press Inc.: New York, New York, 1967; p 3-26.

55. Horiuti, J.; Polanyi, M., A Catalysed Reaction of Hydrogen with Water. *Nature* **1933,** *132* (3343), 819-819.

56. Farkas, A.; Farkas, L., The mechanism of some catalytic exchange reactions of heavy hydrogen. *Transactions of the Faraday Society* **1937,** *33* (0), 678-690.

57. Maxted, E. B.; Moon, C. H., 338. The kinetics of the adsorption of hydrogen and of deuterium by platinum. *Journal of the Chemical Society (Resumed)* **1936,** (0), 1542-1546.

58. Ramachandran, P.; Chaudhari, R., *Three-phase catalytic reactors*. Gordon & Breach Science Pub: 1983; Vol. 2.

59. Jaganathan, R.; Ghugikar, V. G.; Gholap, R. V.; Chaudhari, R. V.; Mills, P. L., Catalytic Hydrogenation of p-Nitrocumene in a Slurry Reactor. *Industrial & Engineering Chemistry Research* **1999,** *38* (12), 4634-4646.

60. Chaudhari, R. V.; Gholap, R. V.; Emig, G.; Hofmann, H., Gas-liquid mass transfer in "dead-end" autoclave reactors. *The Canadian Journal of Chemical Engineering* **1987,** *65* (5), 744-751.

61. McGill, H. L.; Sibbitt, W.; Wiskind, H.; Suciu, S. *HEAT TRANSFER FINAL TECHNICAL REPORT... FEBRUARY 16, 1950, TO FEBRUARY 15, 1951*; Purdue Univ.: 1951.

62. Young, C., IUPAC Solubility Data Series: Hydrogen and Deuterium, Vol. 5/6. Pergamon, New York: 1981.

63. Pray, H. A.; Schweickert, C. E.; Minnich, B. H., Solubility of Hydrogen, Oxygen, Nitrogen, and Helium in Water at Elevated Temperatures. *Industrial & Engineering Chemistry* **1952,** *44* (5), 1146-1151.

64. Sano, Y.; Yamaguchi, N.; Adachi, T., MASS TRANSFER COEFFICIENTS FOR SUSPENDED PARTICLES IN AGITATED VESSELS AND BUBBLE COLUMNS. *Journal of Chemical Engineering of Japan* **1974,** *7* (4), 255-261.

65. Cussler, E. L., *Diffusion: mass transfer in fluid systems*. Cambridge university press: 2009.

66. Evonik AEROXIDE® TiO2 P 25. https://products-re.evonik.com/lpa-productfinder/page/productsbytext/detail.html?xd_co_f=MmY2OGEyYmQtN2Q2ZS00YjdlLWJlNjQtMzU3NDUyNTUzODUz&channel=aerosil&pid=1822&lang=en (accessed May 28, 2019).

67. Crittenden, J. C.; Trussell, R. R.; Hand, D. W.; Howe, K. J.; Tchobanoglous, G., *MWH's water treatment: principles and design*. John Wiley & Sons: 2012.

68. Bates, R. L.; Fondy, P. L.; Corpstein, R. R., Examination of Some Geometric Parameters of Impeller Power. *Industrial & Engineering Chemistry Process Design and Development* **1963,** *2* (4), 310-314.

69. Westheimer, F. H., The Magnitude of the Primary Kinetic Isotope Effect for Compounds of Hydrogen and Deuterium. *Chemical Reviews* **1961,** *61* (3), 265-273.

70. Lee, I., Secondary kinetic isotope effects involving deuterated nucleophiles. *Chemical Society Reviews* **1995,** *24* (3), 223-229.

71. Dougherty, D. A.; Anslyn, E. V. *Modern Physical Organic Chemistry. University Science*; ISBN 1-891389-31-9: 2005.

72. Scott, S. L., The Burden of Disproof. *ACS Catalysis* **2019,** *9* (5), 4706-4708.

73. Micromeritics, A., 2020 Accelerated Surface Area and Porosimetry System Operator's Manual. Micromeritics Instrument Corporation, Norcross, GA: 2003.

74. Micromeritics, A., 2020 Chemi Accelerated Surface Area and Porosimetry System Operator's Manual. Micromeritics Instrument Corporation, Norcross, GA: 2003.

Appendix

Appendix A: Gas Chromatography

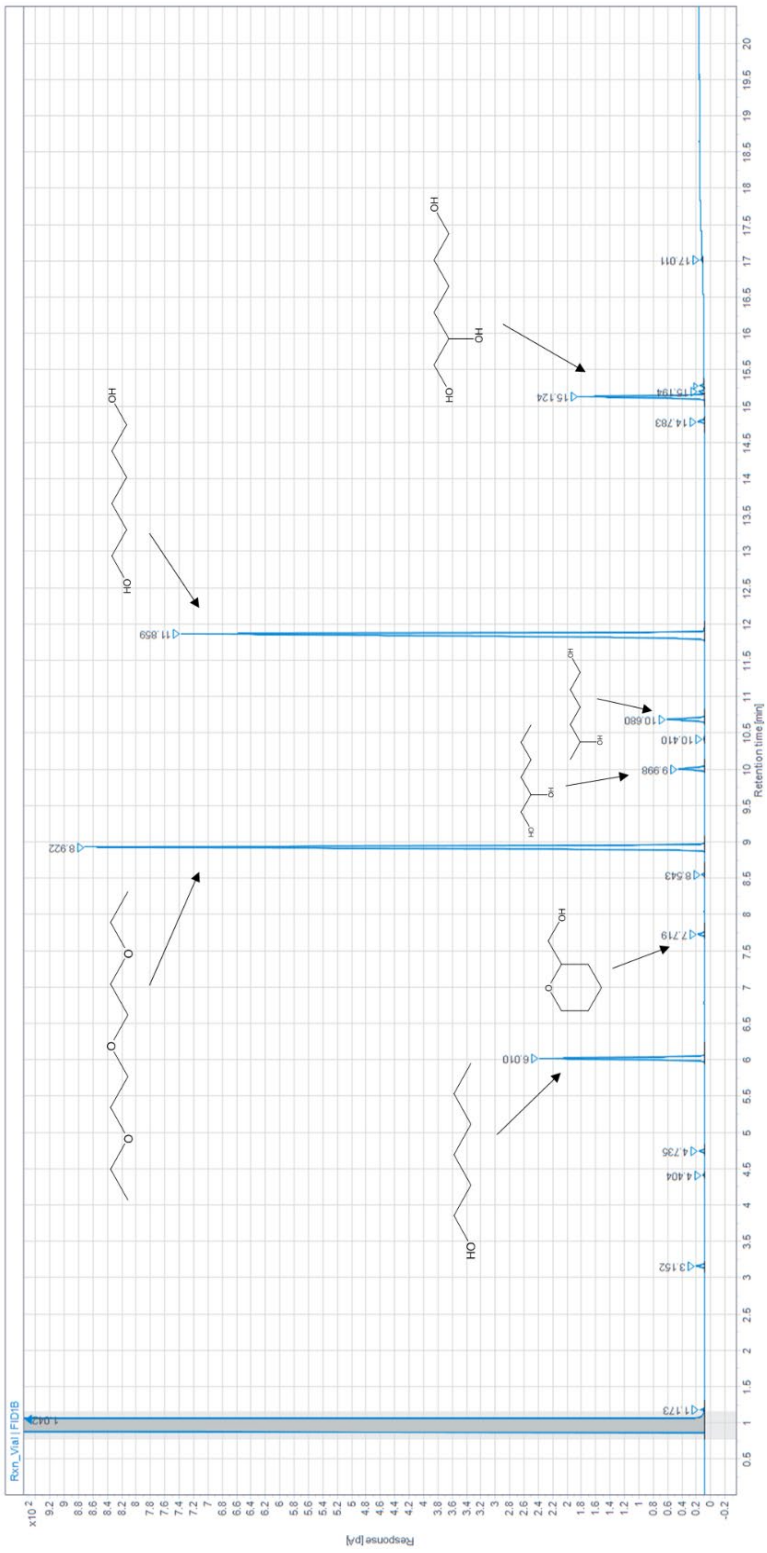

Figure A.1: Gas chromatogram of product solution of a 1,2,6-hexanetriol hydrodeoxygenation reaction with peaks labeled with their corresponding compound found by calibrations.

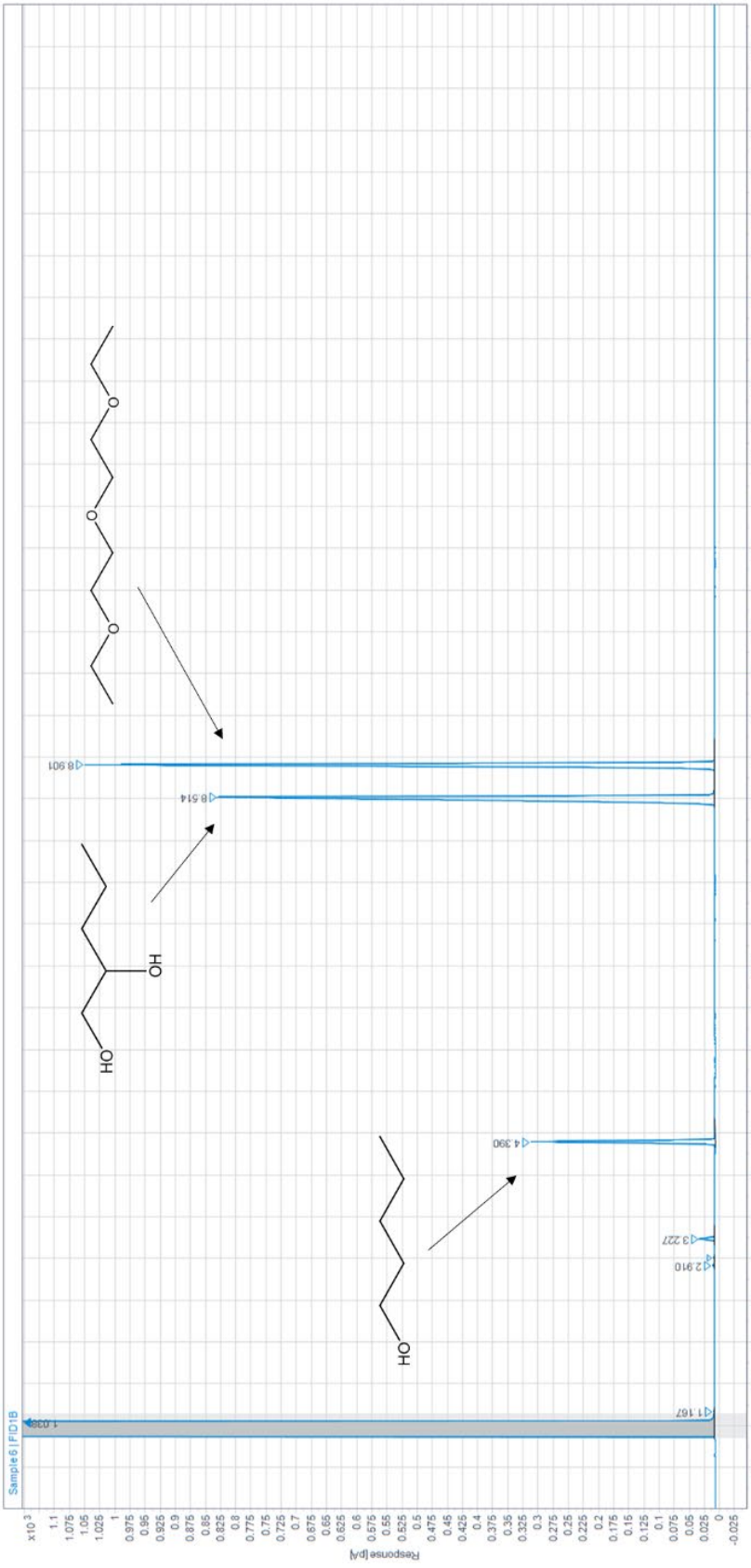

Figure A. 2: Gas chromatogram of product solution of a 1,2-pentanediol hydrodeoxygenation reaction with peaks labeled with their corresponding compound found by calibrations.

Appendix B: Nuclear Magnetic Resonance Spectroscopy

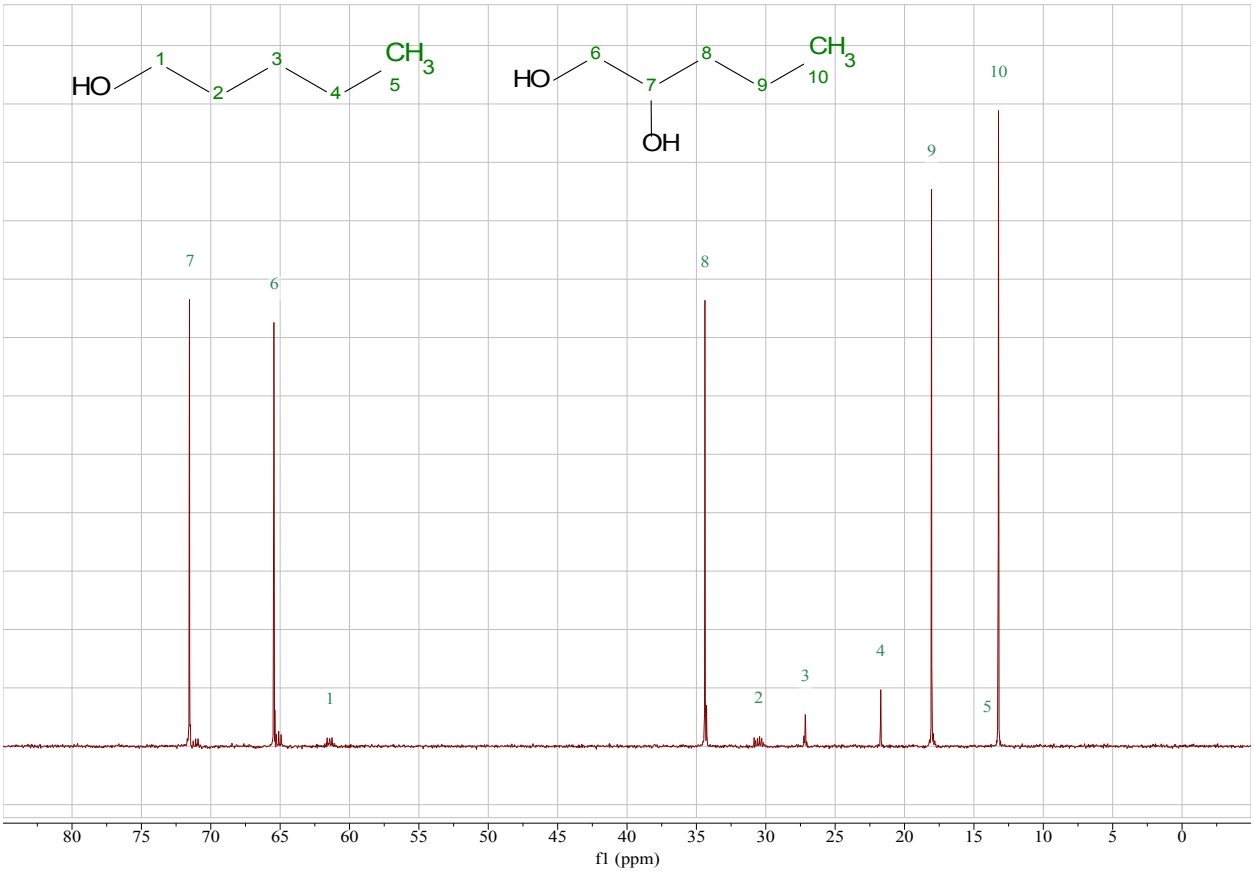

Figure A.3: ^{13}C spectrum for 1,2-pentanediol hydrodeoxygenation-deuterium incorporation experiment. Products with peak assignment for 1-pentanol and 1,2-pentanediol. The peak corresponding to 5-C is a small peak overlapping the 10-C peak located ~13 ppm.

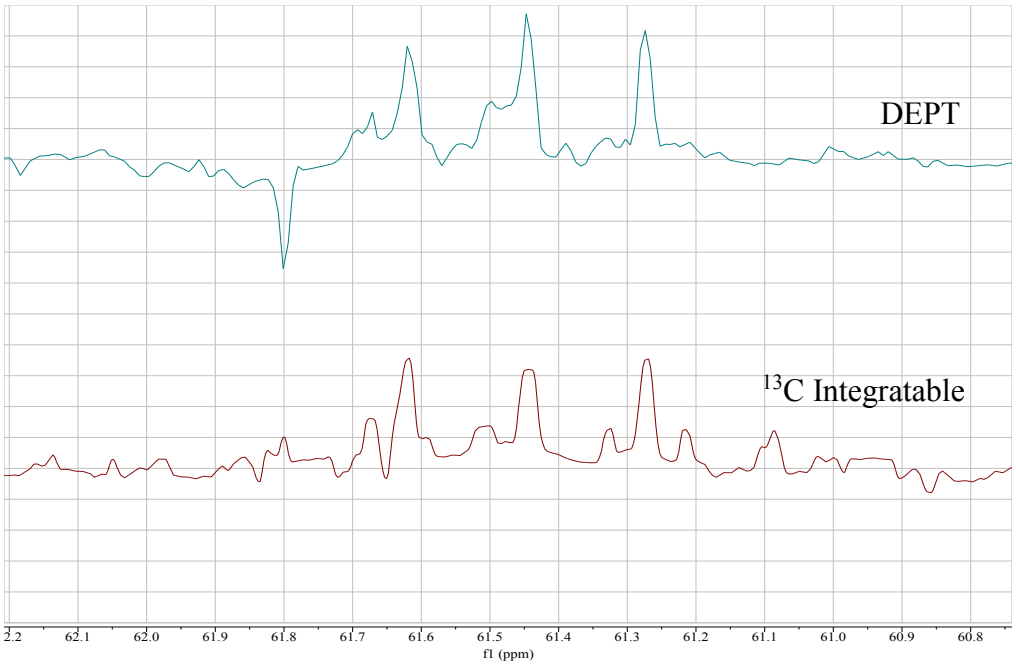

Figure A.4: DEPT and ^{13}C NMR of the α-C of pentanol after hydrodeoxygenation of 1,2-pentanediol with the H_2/D_2O reaction system.

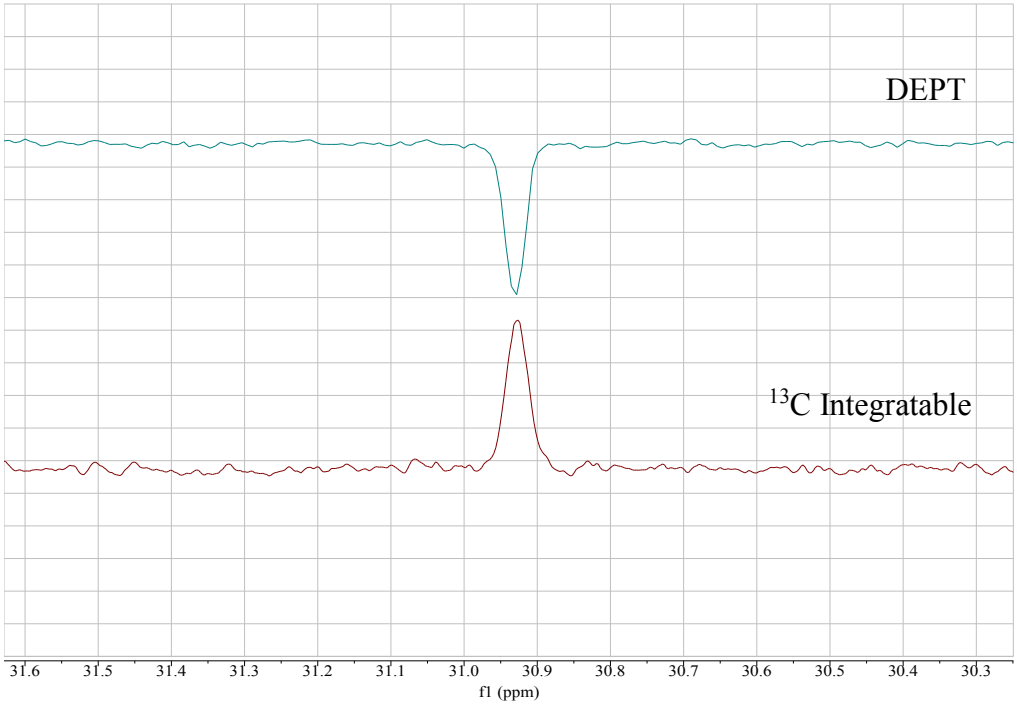

Figure A.5: DEPT and ^{13}C NMR of the β-C of pentanol after hydrodeoxygenation of 1,2-pentanediol with the D_2/H_2O reaction system.

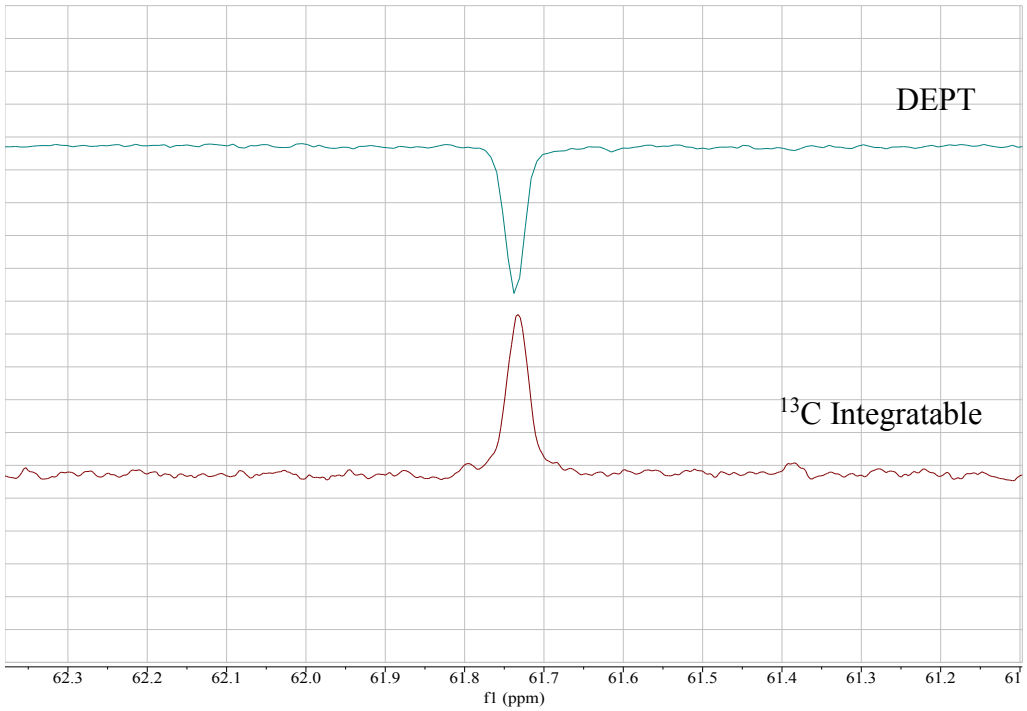

Figure A.6: DEPT and ^{13}C NMR of the α-C of pentanol after hydrodeoxygenation of 1,2-pentanediol with the D_2/H_2O reaction system.

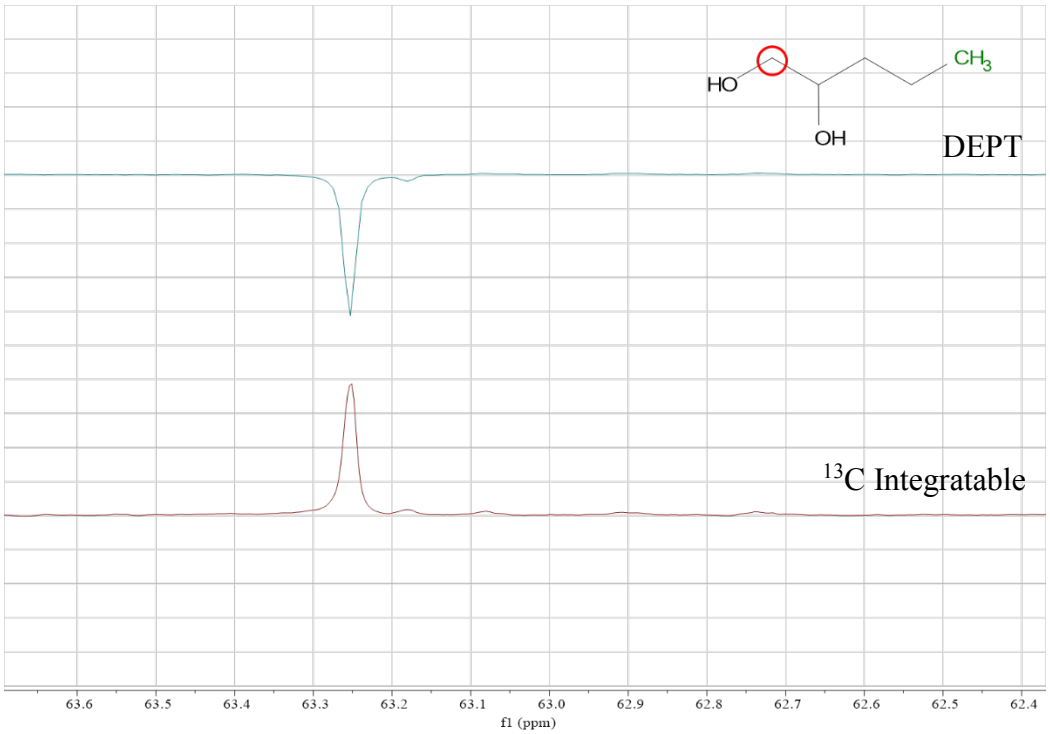

Figure A.7: DEPT and ^{13}C NMR of the α-C of 1,2-PD after hydrodeoxygenation in H_2/D_2O reaction system.

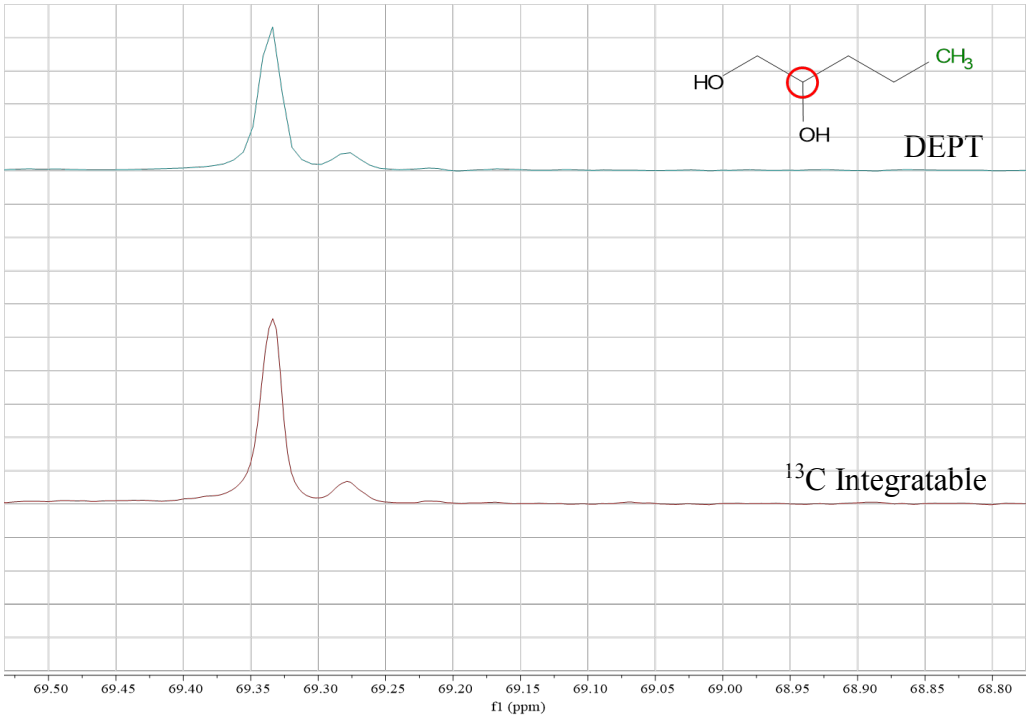

Figure A.8: DEPT and ^{13}C NMR of the β-C of 1,2-PD after hydrodeoxygenation in H2/D2O reaction system.

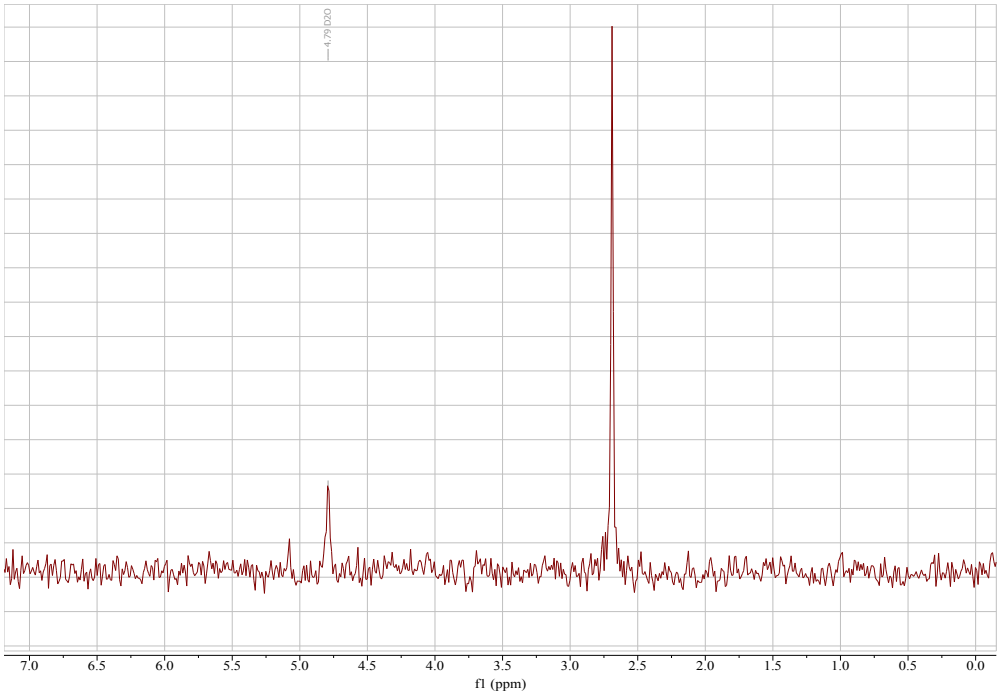

Figure A.9: ^{2}H NMR spectrum of isotopic exchange experiment between only D_2 and H_2O. Peak at ~4.8 is DHO and the peak at ~2.7 is DMSO-d_6.

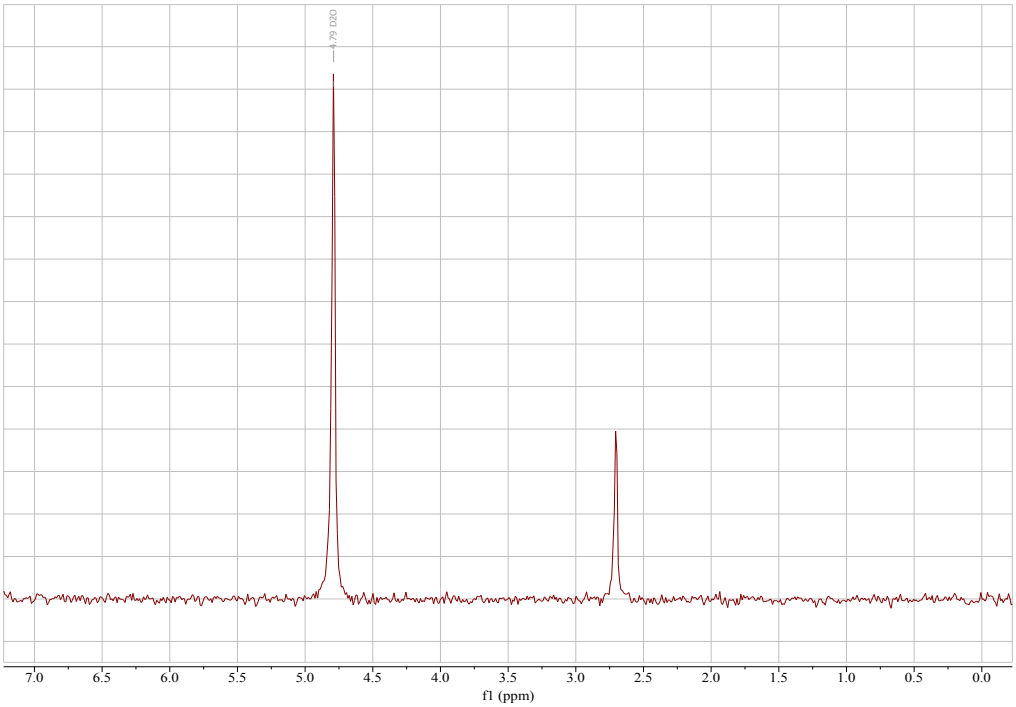

Figure A.10: ^{2}H NMR spectrum of isotopic exchange experiment between D_2 and H_2O in the presence of the Pt-WO_x/TiO_2 catalyst. Peak at ~4.8 is DHO and the peak at ~2.7 is DMSO-d_6.

Appendix C: Powder X-Ray Diffraction

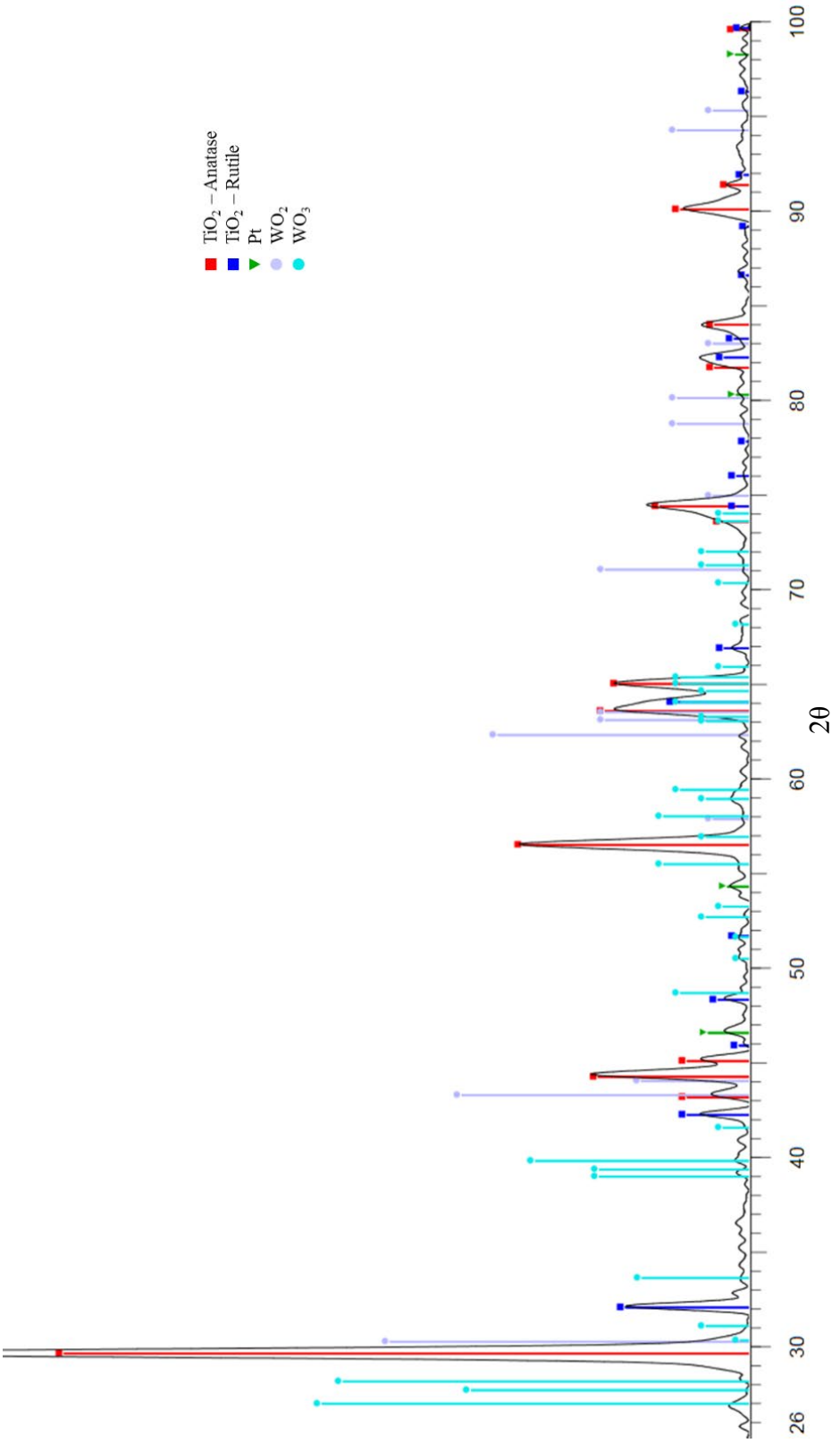

Figure A.11: PXRD of Pt-WO_x/TiO_2 catalyst with peak profile fitting for TiO_2 - anatase (PDF 4-0477), TiO_2 - rutile (PDF 21-1276), Pt (PDF 4-0802), WO_2 (PDF 2-0414), and WO_3 (PDF 20-1324).

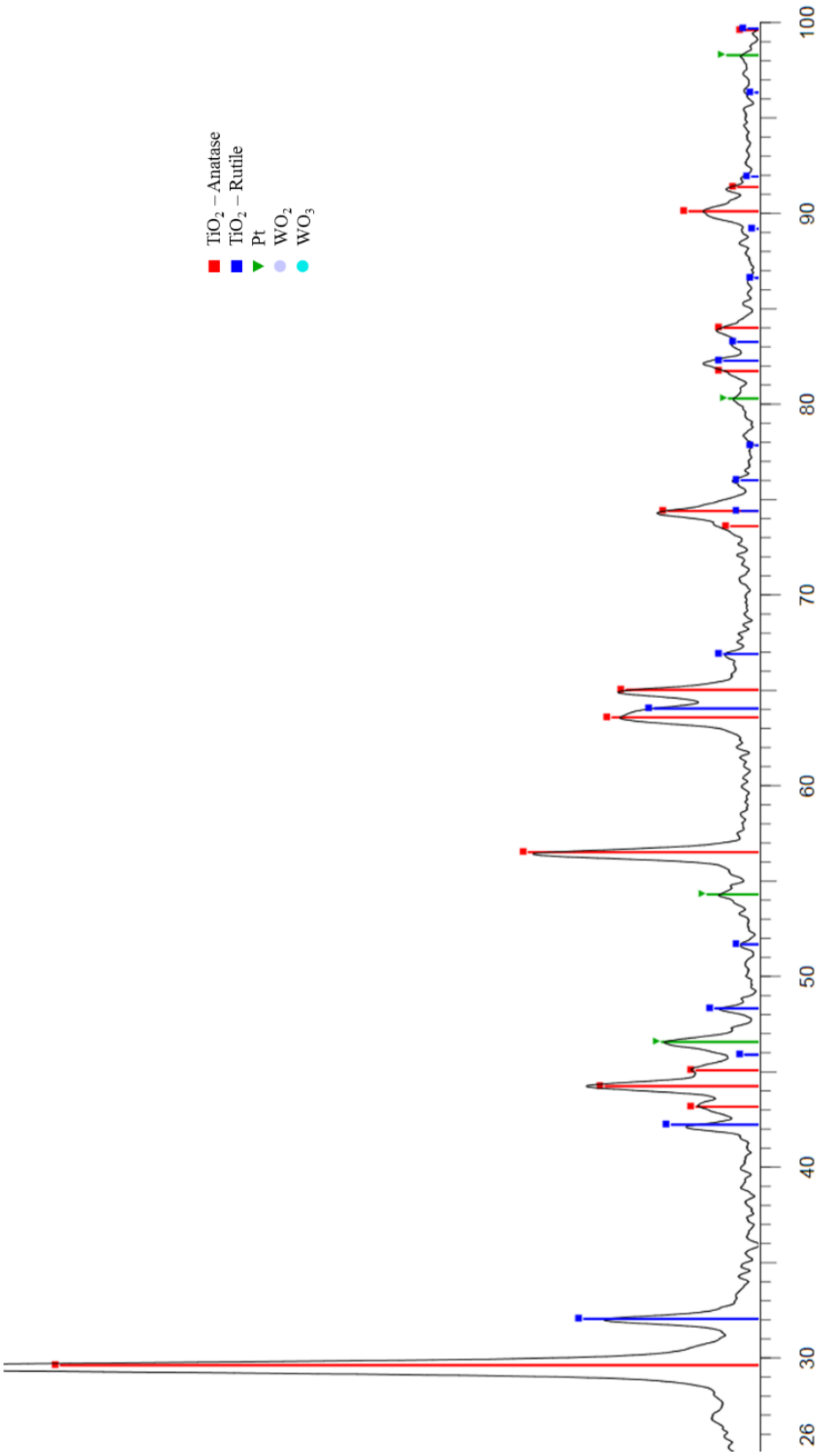

Figure A.12: PXRD of 4 wt% Pt/TiO_2 catalyst with peak profile fitting for TiO_2 - anatase (PDF 4-0477), TiO_2 - rutile (PDF 21-1276), and Pt (PDF 4-0802).

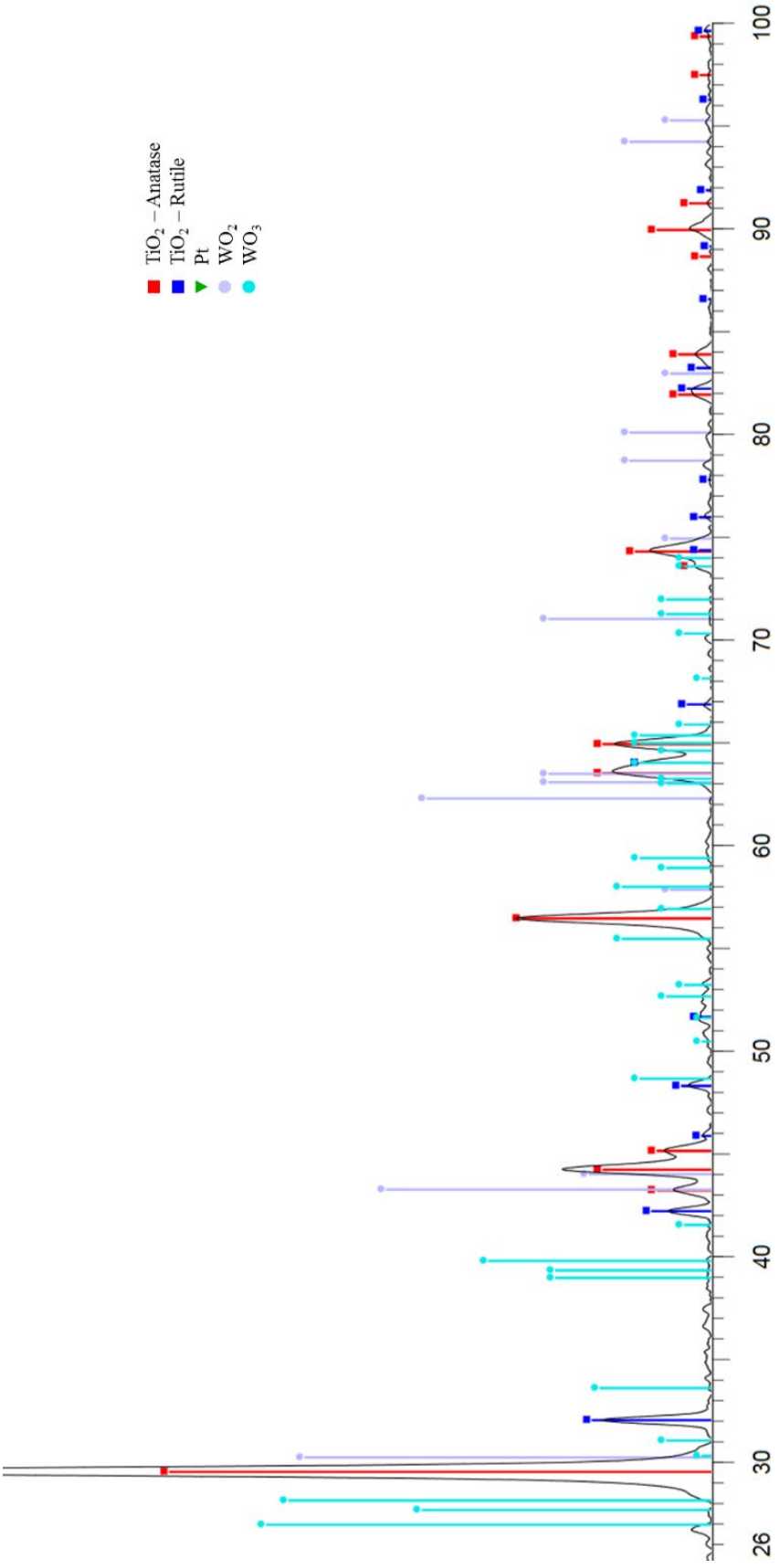

Figure A.13: PXRD of WO_x/TiO_2 catalyst with peak profile fitting for TiO_2 - anatase (PDF 4-0477), TiO_2 - rutile (PDF 21-1276), WO_2 (PDF 2-0414), and WO_3 (PDF 20-1324).

Appendix D: Scanning and Transmission Electron Microscopy

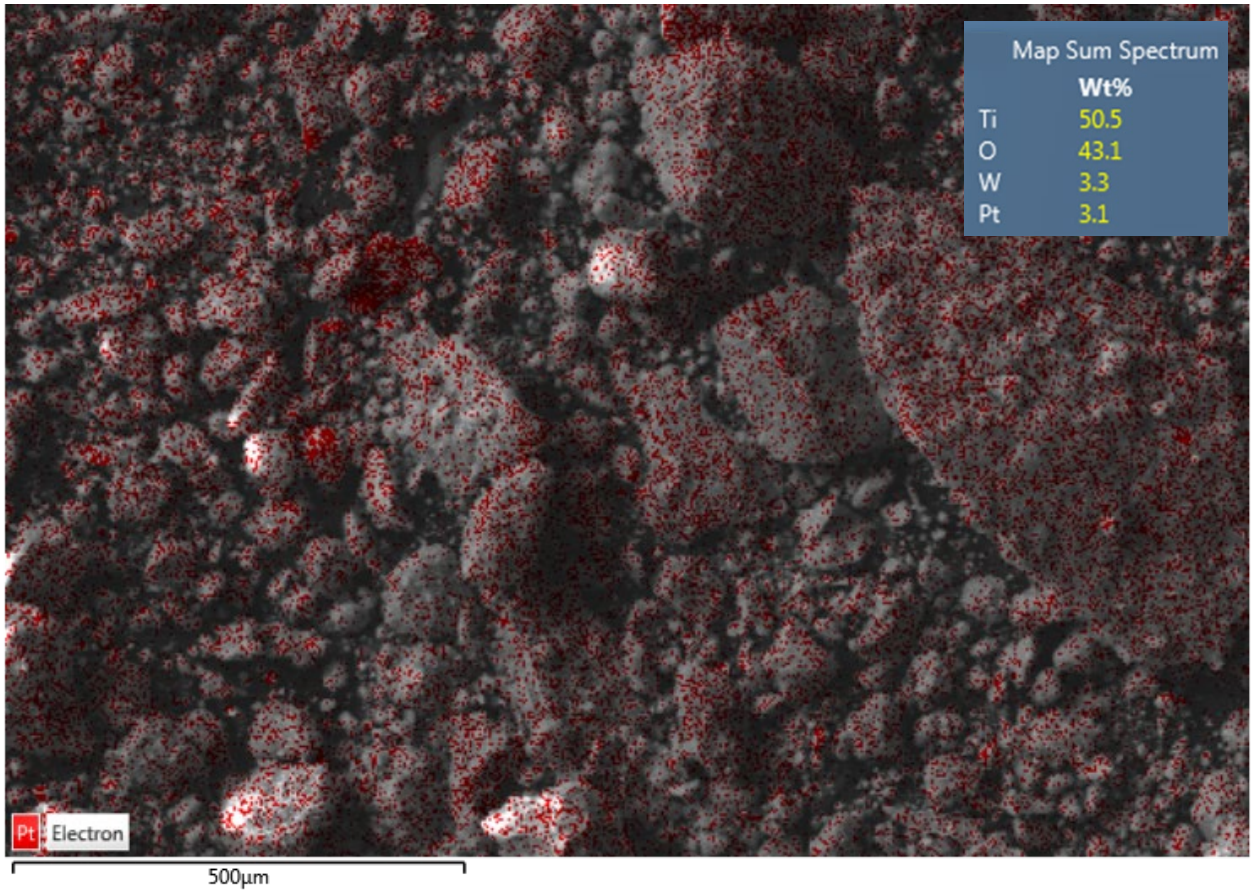

Figure A.14: SEM of Pt-WO_x/TiO_2 catalyst with Pt elemental overlay and EDS elemental analysis results.

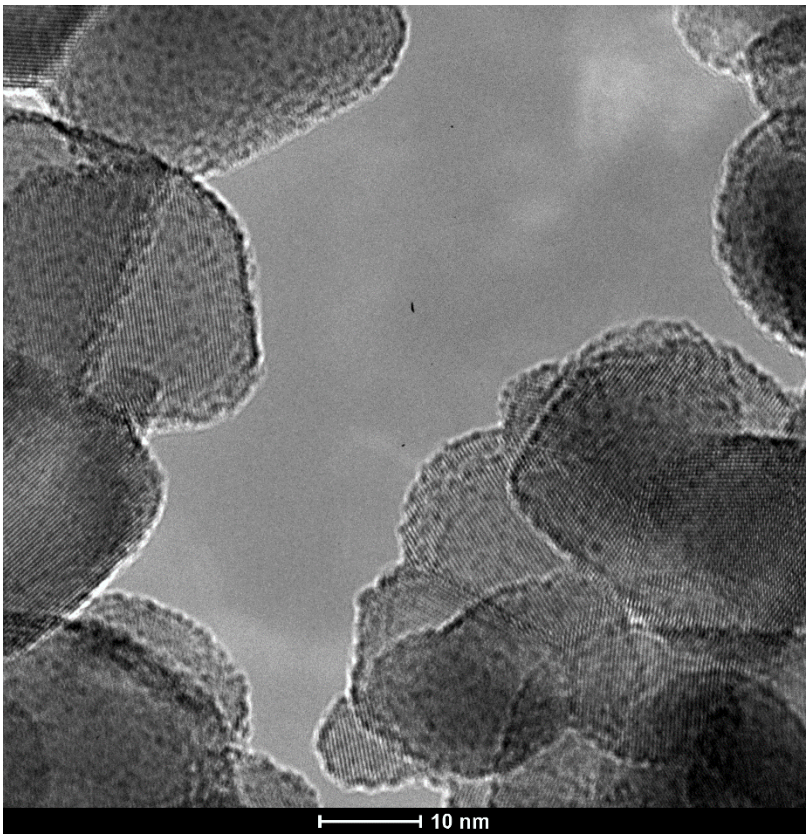

Figure A.15: TEM of WO_x/TiO_2 catalyst showing the subnanometer WO_x particles.

Appendix E: N_2 Physisorption

BET surface area equations:[73]

The BET transformation for each data point is

$$B_1 = \frac{P_{rel_I}}{\left(1.0 - P_{rel_I}\right) * N_{ads_I}} \tag{A12}$$

where B_I is in units of g cm^{-3}, $P_{rel\ I}$ is the relative pressure for the I^{th} data point (mmHg), and $N_{ads\ I}$ is the amount of gas adsorbed after equilibrating I^{th} dose (cm^3 STP). This equation is fitted with least-squares on designated ($P_{rel\ I}$, B_I) pairs where $P_{rel\ I}$ is the independent variable and B_I is the dependent variable.

Surface area is calculated with

$$SA_{BET} = \frac{CSA * (6.023\ x\ 10^{23})}{(22414\ cm^3\ STP) * \left(10^{18}\ \frac{nm^2}{m^2}\right) * (S + Y_{INT})} \tag{A13}$$

where SA_{BET} is the BET surface area in $m^2\ g^{-1}$, CSA is the analysis gas molecular cross-sectional area in nm^2, S (slope, g cm^{-3}) and Y_{INT} (Y-intercept, g cm^{-3}) are calculated via Equation A1.

Error of the BET surface area is calculated by the equation:

$$BET_{ERR} = \frac{SA_{BET} * (S_{ERR}^2 + YI_{ERR}^2)^{0.5}}{Y_{INT} + S} \tag{A14}$$

where S_{ERR} (g cm^{-3}), YI_{ERR} (g cm^{-3}), Y_{INT} (Y-intercept, g cm^{-3}), and S (slope, g cm^{-3}) are calculated with Equation A1.

Table A.1 BJH adsorption pore distribution data.

Average pore diameter (Å)	Cumulative pore volume ($cm^3\ g^{-1}$)
816.5	0.140771
480.8	0.255896
362.6	0.289623
295.4	0.313499
240.3	0.332373
151.3	0.360688
107.1	0.368243
82.7	0.371949
66.8	0.374015
55.5	0.375232
47.2	0.376091
40.6	0.376761
35.3	0.377462
30.8	0.378291
27.0	0.379399
23.6	0.380697
20.4	0.381978
17.3	0.382805

Table A.2: BJH desorption pore distribution data.

Average pore diameter (Å)	Cumulative pore volume ($cm^3\ g^{-1}$)
836.9	0.011307
571.4	0.048103
377.0	0.213081
292.0	0.26766
239.6	0.31019
156.2	0.36809
108.6	0.380394
80.5	0.383789
63.5	0.384141
22.9	0.38421
19.8	0.384303

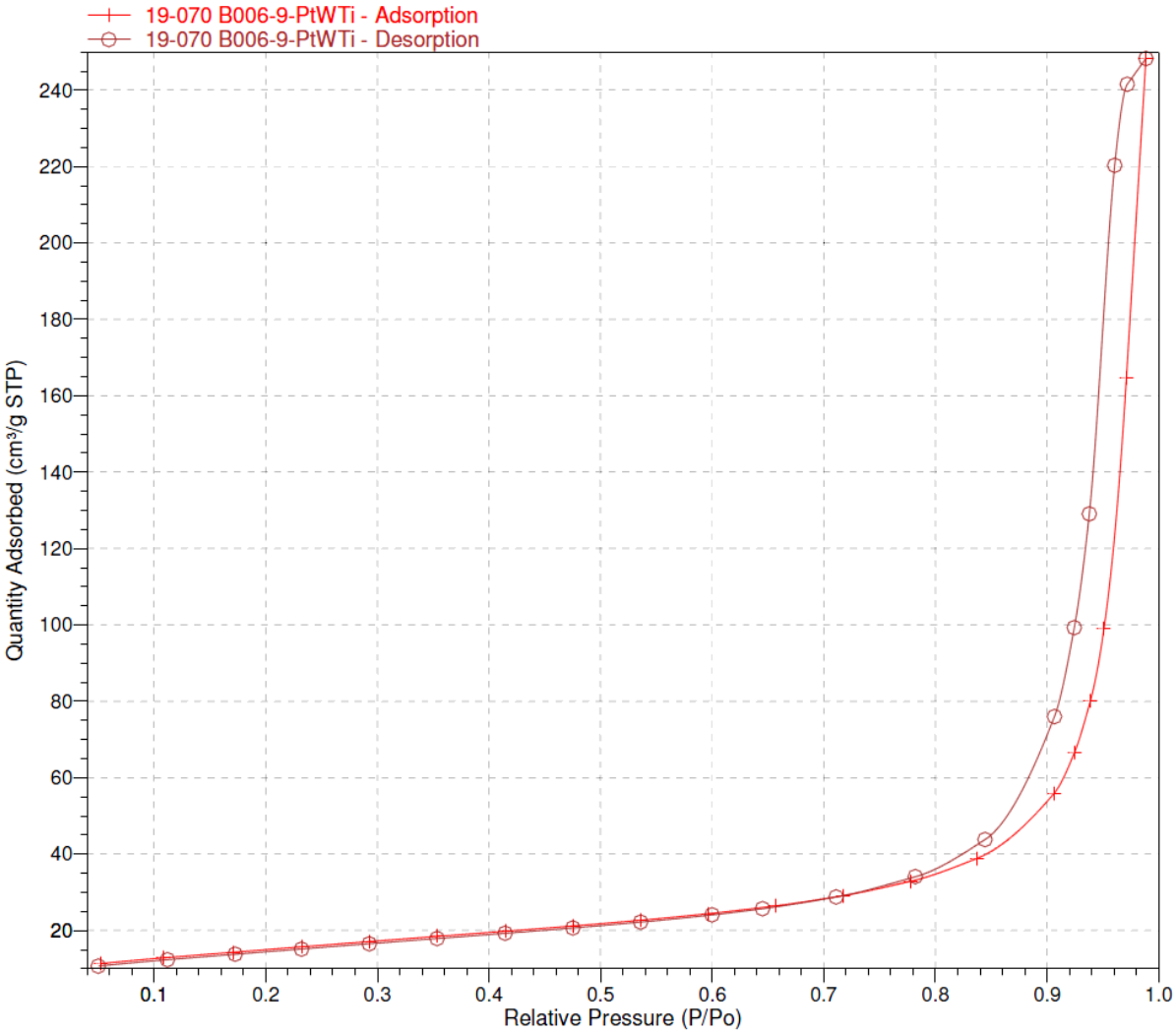

Figure A.16: N_2 physisorption linear isotherm plot for analysis of 4 wt% Pt-WO_x/TiO_2.

Appendix F: CO Chemisorption

Equations used:[74]

The platinum metal dispersion was found by the equation

$$\%M_{DISP} = \frac{100\% * 100\%}{22414} * \frac{V * SF_{CALC}}{\frac{\%weight}{W_{ATOMIC}}} \quad \text{(A15)}$$

where $\%M_{DISP}$ is the metal dispersion (%), V is the volume intercept derived from the best fit line to the volume differences between the selected points of the first analysis and the repeat analysis, SF_{CALC} is the calculated stoichiometry factor, %weight is the percent of sample weight for the metal, and W_{ATOMIC} is the atomic weight of the metal (g mol^{-1}).

The metallic surface area of platinum was calculated with

$$M_{sa} = \frac{6.023\ x\ 10^{23}}{22414} * V * SF_{CALC} * A_{AREA} \quad \text{(A16)}$$

where M_{sa} is the metallic surface area in m^2 g-$sample^{-1}$, V and SF_{CALC} are defined as before, and A_{AREA} is the effective area of 1 active metal atom (m^2 $atom^{-1}$).

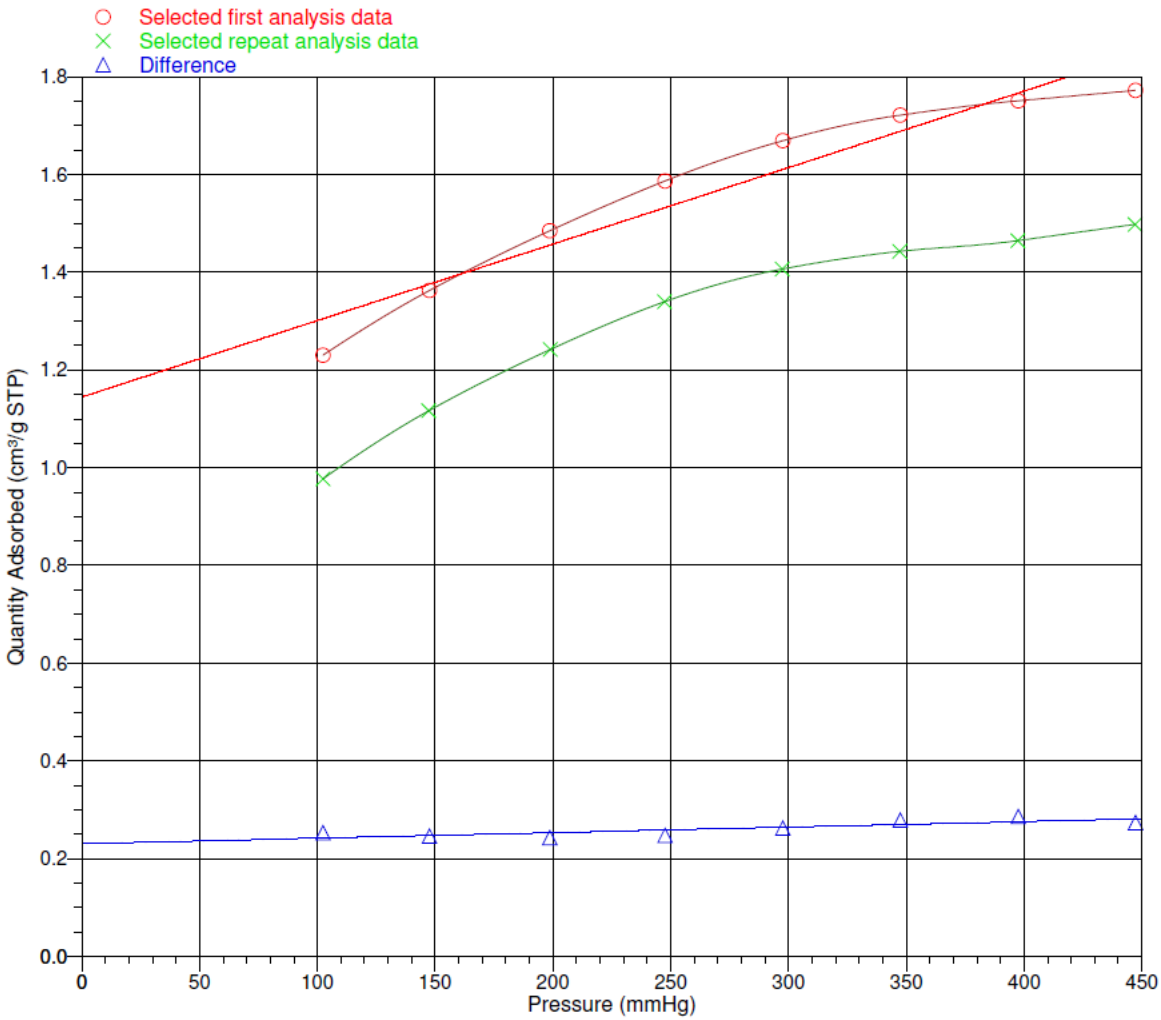

Figure A.17: Isotherm plot from CO chemisorption experiment of the Pt-WO_x/TiO_2 catalyst. A repeat analysis is done to subtract the physisorbed CO to obtain a value that represents chemisorbed CO exclusively.

Table A.3: Experiment log of CO chemisorption experiment for Pt-WOx/TiO2 catalyst.

Task Number	Task Name	Start Time (h:min)	Gas	Furnace Temp. (℃)	Sample Temp. (℃)	Time (min)	Pressure (mmHg)
1	EVAC	0:02	Hel	125.6	99.5	30	
2	FLOW	0:56	H2	127.4	96.5	5	749.5400
3	FLOW	1:02	H2	422.7	350.2	120	751.6200
4	EVAC	3:31		418.3	350.5	30	
5	EVAC	4:04		40.0	34.6	30	
6	LEAK	6:58		40.4	35.1	1	
7	EVAC	7:02		35.9	34.8	30	
8	ANL	7:32	CO	40.1	35.8	171	440.1446

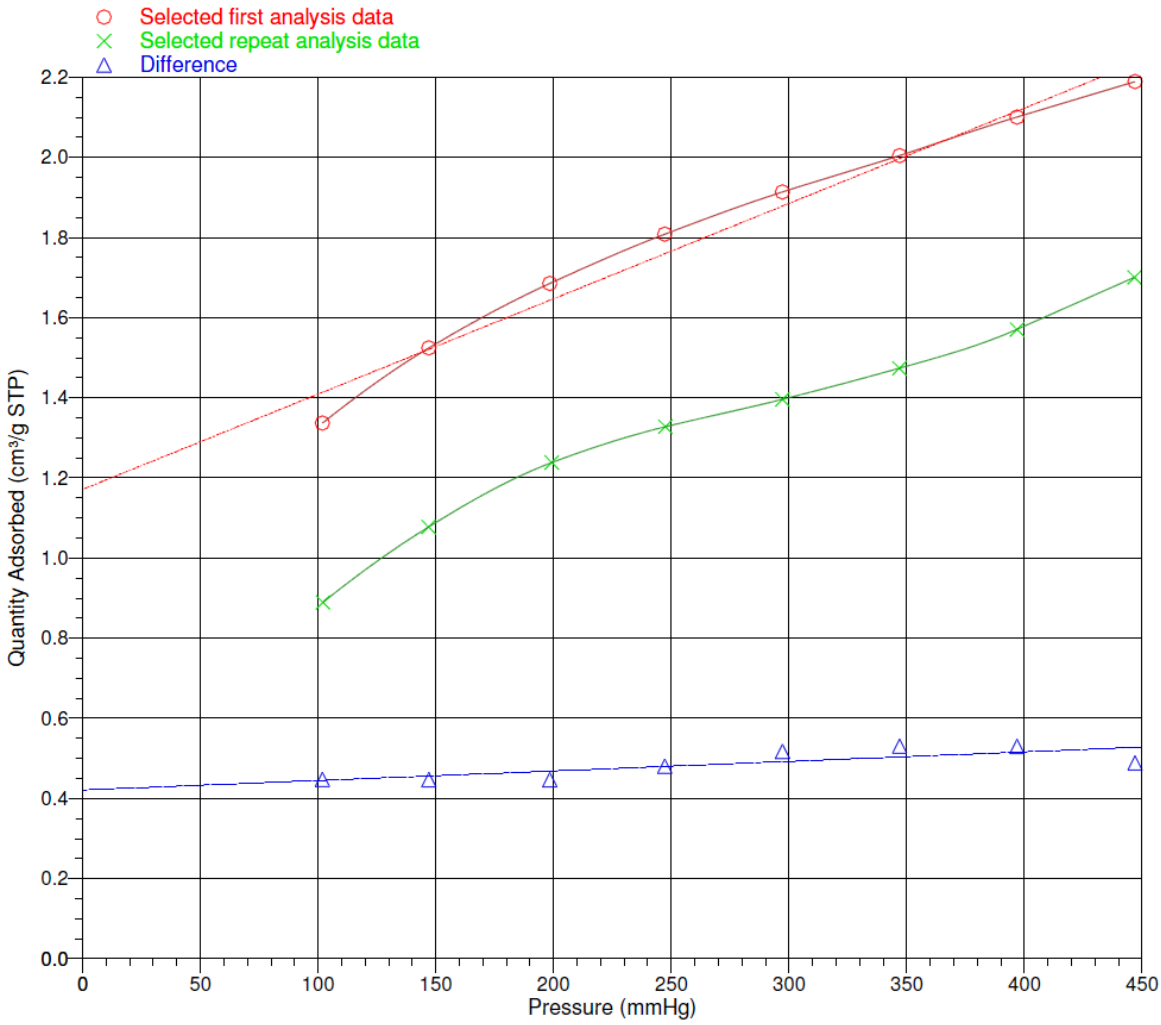

Figure A.18: Isotherm plot from CO chemisorption experiment of the Pt/TiO_2 catalyst. A repeat analysis is done to subtract the physisorbed CO to obtain a value that represents chemisorbed CO exclusively.

Table A.4: Experiment log of CO chemisorption experiment for Pt/TiO_2 catalyst.

Task Number	Task Name	Start Time (h:min)	Gas	Furnace Temp. (℃)	Sample Temp. (℃)	Time (min)	Pressure (mmHg)
1	EVAC	0:02	Hel	130.9	100.0	30	
2	FLOW	0:49	H2	133.3	98.5	5	759.7100
3	FLOW	0:56	H2	428.9	350.0	120	762.9200
4	EVAC	3:23		424.7	350.2	30	
5	EVAC	3:56		40.1	35.0	30	
6	LEAK	6:52		39.1	35.1	1	
7	EVAC	6:56		39.6	35.0	30	
8	ANL	7:27	CO	37.5	34.4	178	437.5738

Appendix G: Kinetic Isotope Effects

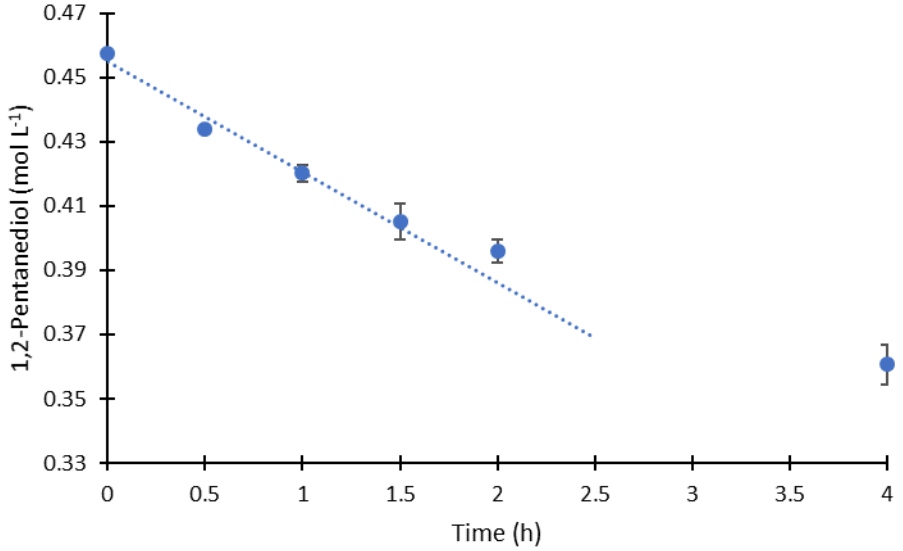

Figure A.19: Concentration of 1,2-pentanediol as a function of time with a straight line fit on the first four data points for reaction in the stirred tank reactor with substrate solution (5 wt% 1,2-pentanediol in H_2O, 25 mL) under 50 bars H_2 at 180 °C over 1.0 g 4 wt% Pt-WO_x-TiO_2 (1:1).

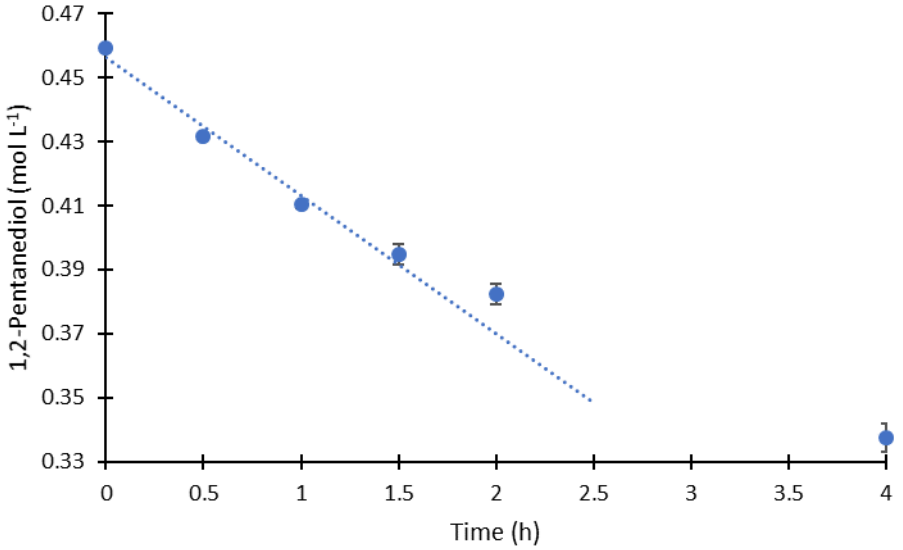

Figure A.20: Concentration of 1,2-pentanediol as a function of time with a straight line fit on the first four data points for reaction in the stirred tank reactor with substrate solution (5 wt% 1,2-pentanediol in D_2O, 25 mL) under 50 bars D_2 at 180 °C over 1.0 g Pt-WO_x-TiO_2.

Error calculations:

The error for each data point found in reaction data and KIE results is calculated with the standard error of the mean:

$$\sigma_m = \frac{\sigma}{\sqrt{n}} \tag{A17}$$

where σ is the standard deviation and n is the sample size. The standard deviation is calculated by the equation

$$\sigma = \sqrt{\frac{\sum(x - \bar{x})^2}{n}} \tag{A18}$$

where x is a data point and $\bar{x}$ is the mean of the data points. For Figure in section 3.5, each data point was taken as the natural logarithm of 1,2-pentanediol concentration while just the concentration of 1,2-pentanediol was used for Figures A.19 and A.20.